



# Decoding the nature of Coherent radio emission in Pulsars I: Observational constraints

Dipanjana Mitra <sup>1,2,\*</sup> , Rahul Basu <sup>2</sup>  and George I Melikizde <sup>2,3</sup> 

<sup>1</sup> National Centre for Radio Astrophysics, Tata Institute of Fundamental Research, Pune 411007, India.

<sup>2</sup> Janusz Gil Institute of Astronomy, University of Zielona Góra, ul. Szafrana 2, 65-516 Zielona Góra, Poland.

<sup>3</sup> Evgeni Kharadze Georgian National Astrophysical Observatory, 0301 Abastumani, Georgia.

\* Correspondence: dmitra@ncra.tifr.res.in

**Abstract:** Radio observations from normal pulsars indicate that the coherent radio emission is excited by curvature radiation from charge bunches. In this review we provide a systematic description of the various observational constraints on the radio emission mechanism. We have discussed the presence of highly polarized time samples where the polarization position angle follow two orthogonal well defined tracks across the profile, that closely match the rotating vector model in an identical manner. The observations also show the presence of circular polarization, with both the right and left handed circular polarization seen across the profile. Other constraints on the emission mechanism is provided by the detailed measurements of the spectral index variation across the profile window, where the central part of the profile, corresponding to the core component, has a steeper spectrum than the surrounding cones. Finally, the detailed measurements of the subpulse drifting behaviour can be explained by considering the presence of non-dipolar field on the stellar surface and the formation of the Partially screened Gap (PSG) above the polar cap region. The PSG gives rise to a non-stationary plasma flow, that has a multi-component nature, consisting of highly energetic primary particles, secondary pair plasma and iron ions discharged from the surface, with large fragmentation resulting in dense plasma clouds and lower density inter-cloud regions. The physical properties of the outflowing plasma and the observational constraints lead us to consider coherent curvature radiation as the most viable explanation for the emission mechanism in normal pulsars, where propagation effects due to adiabatic walking and refraction are largely inconsequential.

**Keywords:** Pulsar; Non-thermal Emission; Radio Emission Mechanism

## 1. Introduction

The discovery of pulsars [1] and their association with rotating neutron stars [2–7] raised questions about the enormously high brightness temperatures ( $\sim 10^{30}$  K) of the radio emission from these sources. These high values exceed all limits of incoherent emission processes and require the presence of a collective or coherent emission mechanism in pulsar [8]. Pulsar radio emission is highly polarized and broadband in nature, usually measured between tens of MHz and tens of GHz. It exhibits a wide range of time dependent phenomena like subpulse drifting, emission mode changing, nulling, microstructures in the single pulses, etc., that pose additional challenges for any proposed model of the coherent emission mechanism.

The pulsar magnetosphere is filled with dense plasma composed of electrons and positrons, and can be divided into open and closed dipolar magnetic field line regions. An outflowing plasma with relativistic energies is expected to stream along the open field line regions where the radio emission is generated [9,10]. Historically, two main classes of coherent radio mechanisms have been distinguished in pulsars: the maser and the antenna mechanisms [11,12]. The maser mechanism requires the development of some plasma instability due to specific distribution function, with likely candidates being the anomalous Doppler effect, the Cherenkov-drift instability, the free electron maser, the inverse Compton

**Citation:** Title. *Journal Not Specified* 2023, 1, 0. <https://doi.org/>

Received:

Revised:

Accepted:

Published:

**Copyright:** © 2024 by the authors. Submitted to *Journal Not Specified* for possible open access publication under the terms and conditions of the Creative Commons Attribution (CC BY) license (<https://creativecommons.org/licenses/by/4.0/>).

scattering, the linear acceleration, etc ([13–19]). The antenna mechanism is conventionally associated with coherent curvature radiation (CCR hereafter). Such division however appear to be quite contrived, since any mechanism has to be associated with some kind of instability in the plasma that is capable of exciting plasma waves. The resulting waves should then escape directly or through other processes from the magnetosphere (see [17]). Despite advances made by these different models the exact process of how the coherent radio emission mechanism operates in pulsar magnetosphere remains hitherto an unsolved and challenging problem. The requirements from observations that can delineate a proper mechanism for pulsar radio emission will be discussed in this article.

The eigen-modes excited in a plasma by any emission mechanism propagate in the medium and eventually detach to reach the observer. The properties of the eigen-modes in strongly magnetized, homogeneous, pair plasma has been relatively well established (see e.g. [20,21]), and briefly summarized from the perspective of pulsars as follows. If the distribution functions of electrons and positrons, the primary constituents of the pulsar plasma, are identical, the dispersion equations describing the system yield two orthogonally polarized modes in the magnetized pair plasma, the ordinary (O-mode) and extraordinary (X-mode) waves. In this work we follow the nomenclature of [22] to describe the eigen-modes in the plasma. The polarization vector of O-mode lies in the plane of the propagation vector,  $\vec{k}$ , and the ambient magnetic field,  $\vec{B}$ , with a component along  $\vec{B}$  as well as  $\vec{k}$ . The X-mode, also known as transverse,  $t$ -mode, has a purely non-potential nature with the polarization vector directed perpendicular to the plane containing  $\vec{k}$  and  $\vec{B}$ . There are two additional branches of the O-mode,  $lt_1$ -mode and  $lt_2$ -mode, that are mixed longitudinal-transverse in nature. If we consider parallel propagation, such that  $\vec{k} \parallel \vec{B}$ , the  $lt_2$ -mode coincides with the Langmuir mode and has a purely potential character. Two limiting frequencies of the Langmuir mode can be found in the observer's frame, when  $k = 0$ , we have  $\omega_1 = \omega_p / \gamma^{1.5}$  while in case of  $k = \omega/c$  one obtains  $\omega_o = 2\sqrt{\gamma} \omega_p$ , here  $\gamma$  is the Lorentz factor,  $\omega_p = \sqrt{2\pi n_p e^2 / m_e}$  is the plasma frequency,  $n_p$  is the plasma density,  $e$  is the electron charge and  $m_e$  is the mass of electrons. Both the  $lt_1$  branch of the O-mode and the X-mode have purely transverse characteristics with the polarization vector either parallel or perpendicular to the  $\vec{k} \times \vec{B}$  plane. The phase velocity of  $lt_1$ -mode is always sub-luminal, while  $lt_2$ -mode is super-luminal for relatively small values of the wave vectors and can be sub-luminal at higher frequencies. The  $t$ -modes are the most suitable candidate for the observed emission, since in presence of strong magnetic fields in the inner magnetosphere where the pulsar radio emission is generated, the  $t$ -modes can escape without any limitations (vacuum like). However for certain excitation mechanisms, the  $t$ -modes encounters difficulties in explaining the observed linear polarization position angle behaviour across the pulse profile, where the position angle closely mimic the change in the magnetic field line planes of a rotating dipole magnet. The difficulty arises because the polarization vector of the  $t$ -mode is perpendicular to the  $\vec{k}$  and  $\vec{B}$  planes, and if the exciting mechanism excites a range of  $k - B$  planes, then the resultant position angle will not follow the change in the magnetic field line planes. A defining attribute of the CCR mechanism is that the waves excited by this mechanism are polarised either perpendicular to the curved magnetic field plane or lies in this plane, and hence CCR can explain the observed position angle behaviour and hence is a strong candidate for pulsar emission mechanism.

There are a number of challenges in finding observational signatures of the emission mechanism due to changes in both the total intensity and polarization behaviour during propagation of the plasma modes in the pulsar magnetosphere. Nonetheless, high detection sensitivity studies of single pulse polarimetric emission from normal pulsars (rotation periods longer than  $\sim 100$  msec) have revealed several details regarding the emission mechanism. In this article we have attempted to highlight some of these observations that provide credible evidence for the radio emission mechanism in normal pulsars to be CCR from charge bunches. These charge bunches excite the linearly polarized  $t$  and  $lt$  modes in

the plasma that can detach from the medium almost instantaneously after excitation, with very little propagation effects in the pulsar plasma. The detected circular polarization in the observed emission requires the presence an additional plasma components in the form of positively charged iron ions. Such ions are naturally generated in the Partially Screened Gap above the pulsar polar cap region. We find effective evidence for Partially Screened Gap from observations of subpulse drifting. We also discuss how the drifting behaviour constrain the surface magnetic field to be non-dipolar in nature.

## 2. Polarization Behaviour in Normal Pulsars

### 2.1. The Rotating Vector Model

A series of papers appeared in 1969 showing the linear polarization position angle (PPA hereafter) to exhibit a characteristic S-shaped sweep across the emission window of a pulsar. These results followed from the radio observations of Vela Pulsar [23] as well as the optical emission from the Crab pulsar [24,25]. The rapid sweep of the PPA strongly suggests a rotational model in pulsars and as a consequence the ‘single-vector’ or the ‘rotating vector’ model (RVM) was proposed where the position angle of the projected single-vector changes due to rotation of the pulsar [23]. The rotation of the position angle has also been observed in Jupiter where the electric field vectors due to synchrotron emission are perpendicular to the magnetic field planes [26] suggesting that the RVM can be generally applied to all such systems (see e.g. [27]). The observations of the Vela pulsar led [23] to conclude that the radio emission originates close to the dipolar magnetic field pole of the neutron star. The strong magnetic field near the magnetic pole rules out synchrotron emission as a possible mechanism leaving curvature radiation from ultra-relativistic charges, moving along curved magnetic field lines, as a viable mechanism [28]. If the curvature radiation is triggered in vacuum the electric field is expected to lie in the plane of the magnetic field. There was also alternative ideas that the observed PPA can be explained from the radiation source being located at the light cylinder [2] or even significantly further away from it [29], see [11] for a detailed review about these early conclusions). However, at these distances the PPA features will be distorted by aberration-retardation effects (see discussion below), thereby ruling out these possibilities.

Generally, the PPA variations in pulsars have a S-shaped sweep resembling the RVM, however, there exists a subset of pulsars with extremely complex PPA behaviour (e.g. [30]). Detailed single pulse studies reveal that part of the complexity seen in average PPA traverse arises due to the presence of orthogonal polarization mode, OPM [31,32]. In several cases the presence of non-orthogonal PPA is also detected. The OPM makes the vacuum curvature radiation model untenable in pulsars [28], with the ordinary and extraordinary mode of the magneto-ionic plasma gaining favourability [33,34]. The non-RVM like PPA behaviour also gives rise to the possibility that radio emission in some pulsars may originate from non-dipolar magnetic fields. But in pulsars where RVM type of PPA traverse is found, clear phenomenological association can be established between the shape of the average profile with the PPA traverse. Using spherical geometry the RVM of PPA traverse can be expressed in the form :

$$\Psi = \Psi_{\circ} + \tan^{-1} \left( \frac{\sin \alpha \sin (\phi - \phi_{\circ})}{\sin (\alpha + \beta) \cos \alpha - \sin \alpha \cos (\alpha + \beta) \cos (\phi - \phi_{\circ})} \right) \quad (1)$$

here  $\Psi$  is the PPA,  $\phi$  is the rotational pulse phase,  $\alpha$  is the angle between the rotation axis and the magnetic axis and  $\beta$  is the angle at closest approach between the rotation axis and the observer line of sight (LOS).  $\Psi_{\circ}$  and  $\phi_{\circ}$  defines the reference points for measurement offsets.

The steepest gradient (SG) point of the PPA lies in the plane containing the rotation and magnetic axis, and is related to  $\alpha$  and  $\beta$  as  $d\Psi/d\phi = \sin(\alpha)/\sin(\beta)$ . Eq. 2 is a purely geometrical construction, and has no provision for interpreting the OPMs (or non-OPMs). In several pulsars two parallel PPA tracks can be found separated by  $90^{\circ}$  in PPA phase, and the same RVM curve can be used for both OPM tracks. Hence, considering RVM to

be a purely geometrical model, it can be seen that large values of  $|d\Psi/d\phi|$  (i.e. low  $\beta$ ) are associated with profiles with multiple components, while small values of  $|d\Psi/d\phi|$  (high  $\beta$ ) is usually found in single component profiles. A statistical study comprising of a significant number of pulsars can be used to construct a two dimensional structure of the emission beam. The best approximation of the average emission beam is believed to comprise of a nested core-cone structure, with a central core emission around the magnetic dipole axis surrounded by two rings of nested conal emission. The average shape depends on the LOS traverse across the emission beam (see discussion in Section 3.1). A number of studies have used the core-cone morphology to obtain a classification scheme for pulsars [35–38], and estimated the location of the radio emission region to be below 10% of the light cylinder radius, consistent with expectations of RVM [23].

## 2.2. Effect of Magnetospheric Plasma on PPA

There are several effects that can change the nature of PPA in the radio emission, like relativistic modifications introduced by rotation, if the source is located close to the light cylinder [39,40], and bending of the dipolar field lines due to sweep-back effects near the light cylinder [41]. It has also been suggested that wave propagation in the magnetospheric plasma can affect the PPA shape [42]. The shift in PPA phases due to aberration retardation effects, arising due to co-rotation of the plasma, has been considered by [43] (BCW hereafter). Other suggested modifications include the effect of return currents [44], and corrections due to the visible point effect, since the LOS is not along the tangent to the magnetic field lines [45,46]. Amongst these, the most prominent feature seen in the observed PPA behaviour is the aberration retardation shifts described by the BCW model, where radio emission is expected to arise from relativistically streaming plasma along the open field lines, and the influence of co-rotating plasma on the RVM is estimated. The particles move along the curved dipolar field lines and due to co-rotation they follow a helical trajectory in the inertial frame. This aberration retardation effect, also called the delay-radius relation, introduces a first order shift in the PPA by an amount  $-3r_{em}/R_{lc}$ , here  $r_{em}$  is the radio emission height,  $R_{lc} = cP/2\pi$  is the light cylinder radius,  $P$  is the rotation period and  $c$  the speed of light. The beaming aberration advances the emission by further  $r_{em}/R_{lc}$ , and hence the total shift between the PPA and the emission window is  $\Delta\phi = 4r_{em}/R_{lc}$ . BCW suggested that  $r_{em}$  can be estimated by measuring  $\Delta\phi$ , defined as the difference between the average pulse profile center and the SG point. This method has been subsequently used to estimate the emission height in a large sample of pulsars, and have constrained radio emission to originate below 10% of the light cylinder radius, i.e.  $\mathcal{R} = r_{em}/R_{lc} < 0.1$ , and matches the geometrical height estimates [37,43,47–58].

At the radio emission heights the first order shifts proposed by BCW dominate over the other distortions [39–41], although the propagation effects in the magnetosphere [42] may introduce comparable changes in  $\Delta\phi$ . The two primary propagation effects are due to refraction and mode coupling. After the emission is generated at  $r_{em}$ , as the waves travel through the distance of the polarization limiting radius,  $r_{pl}$ , their polarization features can change [42,59]. Depending on the mechanism the emission frequency,  $\nu_r$ , is initially either close to or lower than the plasma frequency,  $\nu_p$ . As the wave propagates outwards the plasma density reduces and the value of local plasma frequency decreases. At the height specified by  $r_{pl}$ ,  $\nu_r > \nu_o = 2\sqrt{\gamma_p} \nu_p$  (here  $\nu_o = \omega_o/2\pi$ ,  $\nu_p = \omega_p/2\pi$  and  $\gamma_p$  is the average Lorentz factor of the plasma), and the emission detaches from the magnetosphere as electromagnetic waves. The dispersion relation of the  $t$ -mode has vacuum like characteristics in the medium and as a consequence does not suffer refraction. The  $lt_1$ -mode is sub-luminous with refractive index  $n > 1$ , while the  $lt_2$ -mode comprises of the super-luminous branch with  $n < 1$ , and hence both of them can be subjected to refraction in the medium. The other propagation effect of interest is mode coupling due to “adiabatic walking” [59]. The two natural modes of the plasma propagate independent of each other, but during propagation one of them can generate the other mode and change the intrinsic polarization in a manner such that the polarization vector remains either parallel or perpendicular to the  $\vec{k}$ - $\vec{B}$  plane.

Once the adiabatic walking condition is violated, the modes can couple with each other and emerge as elliptically polarized waves. Thus both refraction and adiabatic walking can cause a twist in the PPA, causing deviation from the RVM. Using typical pulsar parameters BCW concluded that the effect of refraction and mode coupling are small and does not affect the delay-radius relation significantly. This is further supported by the high levels of symmetry in PPA traverse with very close to RVM like behaviour observed in a large number of pulsars. If the radio emission detaches from the pulsar magnetosphere at significantly larger heights, i.e. large  $r_{pl}$ , then due to the co-rotating plasma, the PPA will not be symmetrical in nature. This serves as compelling evidence for the coherent radio emission in pulsars to be generated in the inner magnetosphere, where  $r_{pl}$  is small.

Additional details about the nature of polarization have emerged from observations of the Vela pulsar. The X-ray observation of the pulsar wind nebula has revealed the projection of the rotation axis on to the sky plane [60,61]. The projection of the rotation axis in the plane of the sky makes an angle of  $\sim 90^\circ$  with the projection of the PPA at the SG point, implying that the electric field of the emerging waves is perpendicular to the dipolar magnetic field line planes. If we ignore the propagation effects, the same argument can be extended to the rest of the PPA traverse plane, leading to the conclusion that the emerging radiation is perpendicular to the dipolar magnetic field line planes. The direction of proper motion of the Vela pulsar was found to be along the rotation axis, suggesting that the absolute PPA plane is orthogonal to the direction of motion of the pulsar. In other pulsars the rotation axis cannot be identified, but it is possible to find the direction of proper motion in many cases. The angle between the direction of proper motion and the absolute PPA plane,  $\Delta\Phi_{PM-PA}$ , has a bimodal distribution around  $0^\circ$  and  $90^\circ$  [62–66], and can be interpreted as the polarization of the emerging radiation being either parallel or perpendicular to the magnetic field line planes. However, this conclusion is tentative and the distribution of  $\Delta\Phi_{PM-PA}$  can be easily influenced by several other effects [62,65].

### 2.3. Example of Polarization in Pulsar Radio emission

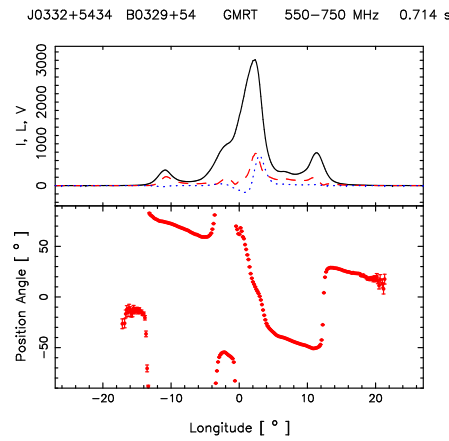


**Figure 1.** The above plot shows the average polarization properties of PSR B0329+54 average over the wideband frequency range between 550 and 750 MHz. The top panel shows the total intensity profile shape (black line), and the variation of the linear polarization (red dashed line) along with circular polarization (blue dotted line) across the profile. The bottom panel shows the average PPA traverse that has quite complex features.

The polarization behaviour in pulsars, as described in the previous section, is illustrated by considering the example of PSR B0329+54 (J0332+5434). The parameters of this pulsar are  $P = 0.715$  s, period derivative  $\dot{P} = 2.05 \times 10^{-15} \text{ s s}^{-1}$ , characteristic age  $5.53 \times 10^6$  years, surface dipolar magnetic field  $1.22 \times 10^{12}$  G and spin-down energy loss of  $2.22 \times 10^{32}$

ergs/s. The average profile has five distinct components and can be classified as Multiple (M) type (see Discussion in Section 3.1). PSR B0329+54 is one of the brightest pulsars in the northern sky and has been extensively studied over a wide frequency range. We observed the pulsar using the Giant Metrewave Radio Telescope (GMRT), consisting of 30 antennas, with 14 antennas located within a central square kilometer area, while the other 16 antennas are spread out in a Y-shaped array with maximum distance of 27 km [67]. The observations were carried out in the full polar, phased array mode of u-GMRT [68], using the wideband receivers between frequency range of 550 and 750 MHz, and around 7000 single pulses were recorded with a time resolution of 0.327 msec. The average profile is shown in Fig. 1 along with the linear and circular polarization levels across the profile window and the time averaged PPA traverse, that has quite a complex nature unlike the RVM. In fact, in the normal pulsar population the RVM does not fit the average PPA traverse in many pulsars and detailed exercise of fitting the RVM to a large sample of pulsars by [69] showed that the RVM was a good fit for 60% of the pulsars and failed for about 40%.

The complex nature of the average PPA traverse of PSR B0329+54 was first unraveled by [70], as they overlaid the PPAs of single pulses to find two clear tracks separated by  $90^\circ$ , that correspond to the two OPMs, as well as other PPAs outside the two tracks. Later studies at multiple frequencies confirmed the detection of the two OPM in this pulsar [71]. The single pulses also show the mode changing behaviour, where the radio emission switches between two stable states with different profile shapes [72–75], but the PPA behaviour is similar in the two emission modes [76]. Fig 2 shows the single pulse PPA distribution from the u-GMRT observations, with the two PPA tracks clearly visible [70].

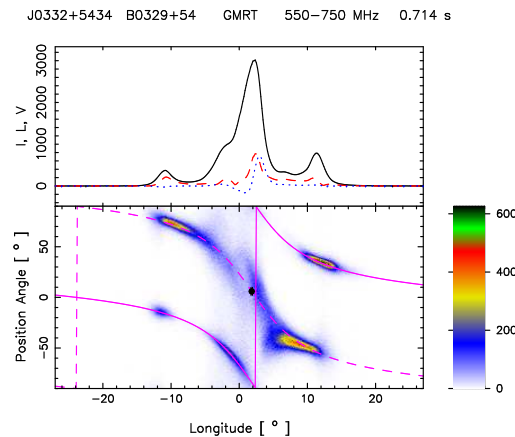


**Figure 2.** The top panel shows the average profile of the total intensity (Stokes I; solid black lines), total linear polarization (dashed red line), and circular polarization (Stokes V; dotted blue line) of PSR B0329+54 between 550 and 750 MHz observing frequency. The lower panel shows the single pulse PPA distribution (color scale) along with the RVM fits to the two PPA tracks, shown as dashed and solid magenta lines.

Subsequent single pulse studies have demonstrated that PPAs of time samples with high levels of linear polarization closely follow the RVM nature [57,77,78]. Fig 3 shows a subset of the PPA behaviour of Fig 2 where the time samples with linear polarization level in excess 90% have been selected. The two PPA tracks of the OPMs are clearly evident in this plot. Each PPA track can be fit with the RVM using the same values of  $\alpha$ ,  $\beta$  and  $\phi_o$ , and tracks are exactly orthogonal. [71] estimated the absolute direction of the PPA with respect to the fiducial plane, containing the rotation axis and the magnetic dipole, and identified the two tracks as the X-mode (dashed magenta line in Fig 2, lower window) and the O-mode (solid magenta line in Fig 2, lower window). The radio emission height can be determined from these observations by estimating the aberration-retardation shifts in the PPA, as discussed in the previous section. We found the shift to be  $\Delta\phi \sim 2^\circ$ , and the

corresponding emission height is about 300 km. In Fig 3 it can be seen that in a narrow region around the longitude  $2^\circ$ , which is also close to the SG point, the average linear polarization level goes below 60%. This is due to the large spread of single pulse PPAs in this longitude range, and we have ignored this narrow region while carrying out the RVM fits. Fig. 4 shows a second subset of the PPA behaviour of Fig 2 where the time samples with linear polarization level less than 30% have been selected. The non-orthogonal PPAs are seen in this figure to be present across the profile.

### 2.3.1. High Levels of Linear Polarization

The presence of individual subpulses with high levels of linear polarization was detected in several earlier studies [79,80], but their origin was unclear. If we consider the situation in Fig 3, where time samples with close to 100% linear polarization levels are shown, the two PPA tracks have identical RVM characteristics with a  $90^\circ$  shift in PPA phase. Although the RVM was proposed for vacuum curvature radiation originating close to the poles of a static magnetic dipole, the two PPA tracks represent plasma effects, and can be associated with the natural plasma modes, i.e.  $t$ -mode and  $lt$ -mode of the pair plasma (see Discussion in section 2.2). However, the  $t$ -mode and  $lt$ -mode are confined to the plasma and additional details are required to understand how they transform into the electromagnetic X and O-modes that can escape the plasma, and yet retain the vacuum like PPA characteristics.

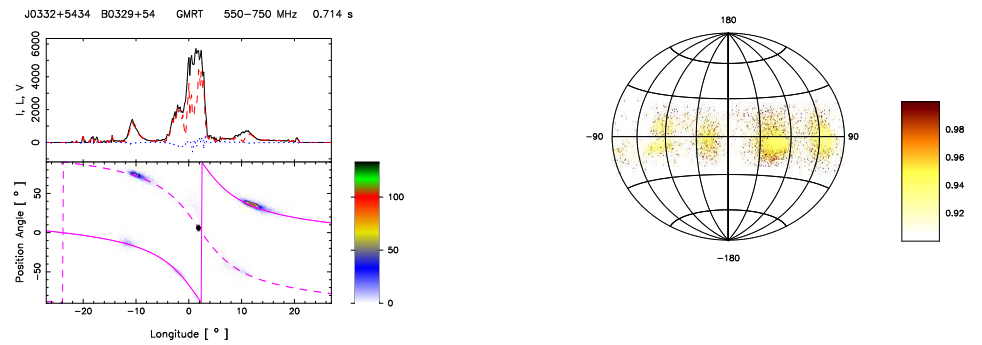


**Figure 3.** The above plot shows a subset of the observed polarization behaviour in PSR B0329+54 for time samples with linear polarization level larger than 90%. In the left window, the top panel shows the average profile with total intensity (Stokes I; solid black lines), total linear polarization (dashed red line), and circular polarization (Stokes V; dotted blue line). The lower panel in the left window shows the single pulse PPA distribution (color scale) with distinct orthogonal tracks. The RVM fits to the PPAs are also shown as dashed and solid magenta lines in this plot. The right plot shows the Hammer–Aitoff projection of the polarized time samples with the color scheme representing the fractional polarization level.

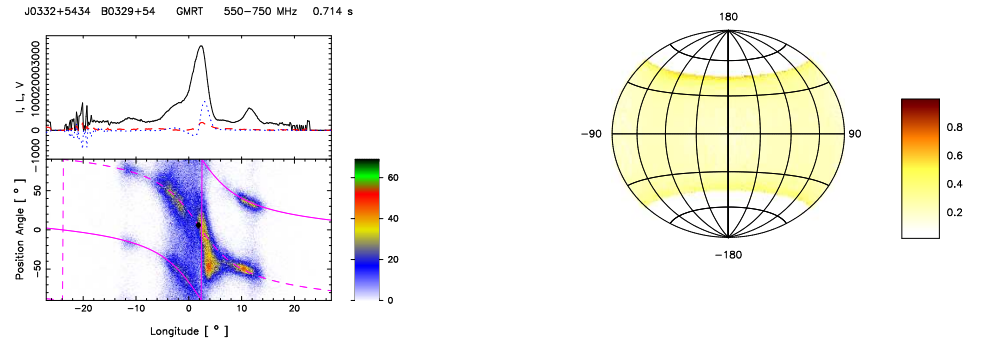


**Figure 4.** The above plot shows a subset of the observed polarization behaviour in PSR B0329+54 for time samples with linear polarization level less than 30%. In the left window, the top panel shows the average profile with total intensity (Stokes I; solid black lines), total linear polarization (dashed red line), and circular polarization (Stokes V; dotted blue line). The lower panel in the left window shows the single pulse PPA distribution (color scale) with non-orthogonal characteristics. The RVM fits to the PPAs are also shown as dashed and solid magenta lines in this plot. The right window shows the Hammer–Aitoff projection of the polarized time samples with the color scheme representing the fractional polarization level.

The  $t$ -mode and  $lt$ -mode have slightly different dispersion relations in the magnetospheric plasma and can propagate independent of each other. It has been noted by [59] that in a slowly varying magnetoionic inhomogeneous plasma the polarization features at the emission region evolves due to adiabatic walking. At a certain distance the effect of adiabatic walking is terminated and the observed polarization behaviour reflects the pattern frozen in at this point. Under these circumstances it is possible to obtain high levels of linear polarization, but the effect of emission mechanism on the PPA is lost. On the contrary the single pulse observations reported in [77] showed that subpulses with high levels of linear polarization had PPAs across them that closely followed the RVM nature. Also in a recent study [81] shows that by applying the high polarized time sample criteria, the RVM can be recovered for a large number of pulsars and for several pulsars the high polarized samples follow two parallel RVM like PPA tracks. These observations hence strongly favour the natural modes in the plasma to be excited by CCR, with the radiation detaching from the magnetosphere almost immediately after they are generated, with little influence of propagation effects like adiabatic walking [82]. Given the fundamental importance of propagation effects on the observed polarization behaviour and their ability to uncover the emission mechanism, we discuss below the possibility in more detail.

### Propagation Effect Cannot Explain the High Levels of Linear Polarization

The aberration and retardation effect is likely to affect both the  $t$ - and  $lt$ -modes propagating in the plasma, and the effect depends on the emission height from which each mode detaches from the plasma. The  $t$ -mode, with vacuum like dispersion property, remains unaffected by refraction in the medium and propagates along the tangent to the magnetic field line at the point of generation. On the other hand both branches of the  $lt$ -mode are refracted in the medium and are ducted along the magnetic field lines with different extents. If the  $t$ -mode and the  $lt$ -mode detach from the magnetosphere at different heights the observed PPA tracks should be different. However, the PPA tracks of the two OPM are observed to be identical, suggesting that the effects of refraction is minimal. As a result we can conclude that the two modes escape the plasma from the same height.



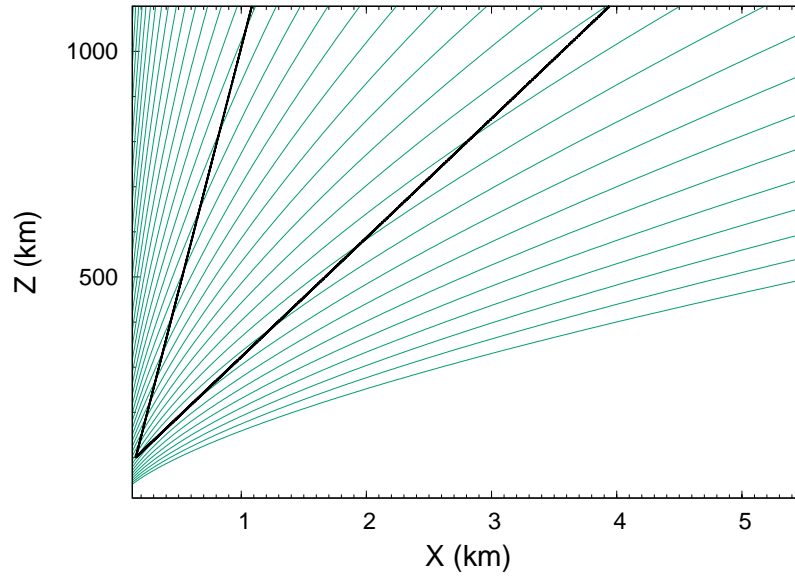


**Figure 5.** The above plot shows the schematic of the open dipolar magnetic field lines (in green) above the neutron star surface. The black diverging lines correspond to the rectilinear propagation vector of an  $1/\gamma_p$  emission cone of  $t$ -mode generated at a height of 100 km from the surface, where  $\gamma_p = 350$ . The radio emission detaches around 1000 km from the surface.

In order to understand the effect of adiabatic walking on the radio emission let us assume the presence of a hitherto unknown mechanism that is capable of exciting the normal modes in the relativistic pair plasma. The emission is confined within a narrow cone ( $\sim 1/\gamma_p$ ) centered around the tangent to local magnetic field. The excitation frequency is close to the plasma frequency and the linear polarization is either parallel or perpendicular to the  $\vec{k} \times \vec{B}$  plane<sup>1</sup>, but when averaged within the cone the emission is completely depolarized. The longitude resolution in Fig. 3 is  $0.16^\circ$ , and if associated with the angular size of the relativistically emitting cone, the corresponding Lorentz factor is  $\gamma_p \sim 350$ . A mechanism to obtain close to 100% linear polarization from the  $1/\gamma_p$  emission cone, based on the adiabatic walking condition, was proposed by [59]. As the radiation propagates, the curved magnetic field lines bend and due to adiabatic walking the emission cone is no longer centered around the tangent to the local field lines, but is directed away from them in its entirety. The polarization vector needs to adjust itself to remain parallel or perpendicular to the  $\vec{k} \times \vec{B}$  plane, and hence in this situation all the polarization vectors within the cone are pointed in the same direction. Hence, the resultant polarization within the emission cone can reach levels close to 100%. This behaviour is illustrated in Fig. 1 of [59], and shows the reorientation of the polarization vector in the emission cone due to adiabatic walking. However, one possible issue in this representation is that the cross-section of the emission cone is assumed to be same at different heights. On the contrary, the cross-section of the cone keeps on increasing as the emission propagates upwards, as shown in Fig. 5 for the  $t$ -mode generated at a height of 100 km above the surface. The black lines in the figure correspond to a  $1/\gamma_p$  cone, with  $\gamma_p \sim 350$ , while green line represent the open magnetic field lines. The radio emission detaches from the plasma at a height of  $\sim 1000$  km, where the diverging field lines are still enclosed by the  $1/\gamma_p$  cone. Any averaging effect within this cone would likely result in complete depolarization of the emission [82]. Similar arguments can be made for the  $lt$ -mode as well.

Thus we conclude that the time samples with high levels of linear polarization seen in Fig. 3 cannot be explained by adiabatic walking. Additionally, the symmetrical nature of the PPA traverse requires extreme fine tuning of the plasma parameters. The multiple com-

<sup>1</sup> For example the linear acceleration mechanism excites the O-mode and has polarization oriented parallel to the  $k - B$  plane

ponents in the profile also suggests the presence of non-stationary plasma flow, and cannot satisfy the conditions for adiabatic walking, i.e. slow change of plasma density. **It should be noted that in average profile the fractional polarization across a wide frequency range can be frequency dependent, where higher frequency tends to have more depolarization (see e.g. [48,83,84]). Generally depolarization is attributed to the mixing of OPMs, and some studies has been devoted to the mechanisms of depolarization ([85,86]), and also their frequency dependent behaviour ([87]). In this context simultaneous wide band observations of high linearly polarized time sample in order to explore their frequency dependence can be quite instructive.**

### High Levels of Linear Polarization from Curvature Radiation

Curvature radiation excites the  $t$  and  $lt$  modes, and due to difference in refractive indices the modes split in the plasma medium and can travel independently as linearly polarized modes, perpendicular and parallel to the curved magnetic field line planes, respectively [88]. There is evidence for the observed PPAs from normal pulsars being either parallel or perpendicular to the curved magnetic field plane. If CCR indeed acts as the radio emission mechanism in pulsars, then several critical conditions related to coherence and escape of waves need to be satisfied. [12] suggested that linear electrostatic Langmuir waves could be a possible source of CCR, but this model was not found to be applicable by [89] (see details in Paper II). An alternative theory has been developed where it was suggested that the modulational instability of Langmuir wave can form charge envelopes, or solitons, that are stable enough to emit CCR [15,90].

[12] also proposed the existence of an inner vacuum gap region above the polar cap where non-stationary plasma flow arises due to intermittent spark discharges and pair plasma cascade, which eventually gives rise to a two stream instability. This model can be used to address a number of observational phenomena such as subpulse drifting, microstructures in the single pulses, and measurements of hot polar cap. However, the vacuum gap model do not quite agree with the details of these measurements and requires modification in the form of a partially screened gap, PSG hereafter [91] (see discussion below in section 4). An illustration of the non-stationary plasma flow from the PSG model is shown in Fig. 6. In the dense pair plasma clouds stable relativistic charged solitons can be generated at distances of few percent of  $R_{lc}$ , that have Lorentz factor  $\Gamma$ , larger than the Lorentz factor of spark-associated plasma  $\gamma_s^{sp}$ . The solitons while moving along the curved magnetic field lines excite CCR with characteristic frequency,  $\nu_r \sim 1.2c\Gamma^3/2\pi\rho \sim 0.8 \times 10^{-9}(\Gamma^3/P)\mathcal{R}^{-0.5}$ , where  $\rho \sim 2(r_{em}R_{lc})^{0.5}$  is the radius of curvature of the open dipolar field lines. If we use the parameters of PSR B0329+54, and assume typical values of  $\mathcal{R} \sim 0.01$ ,  $\Gamma \sim 300$  we get  $\nu_r \sim 0.4$  GHz, which lies in the typical radio frequency range. Using multiplicity factor of the spark-associated plasma,  $\kappa^{sp} \sim 10^4$ , the characteristic frequency  $\nu_o \sim 2.4 \times 10^{11} \text{ s}^{-1}$  satisfies the condition  $\nu_r \ll \nu_o$  in PSR B0329+54.

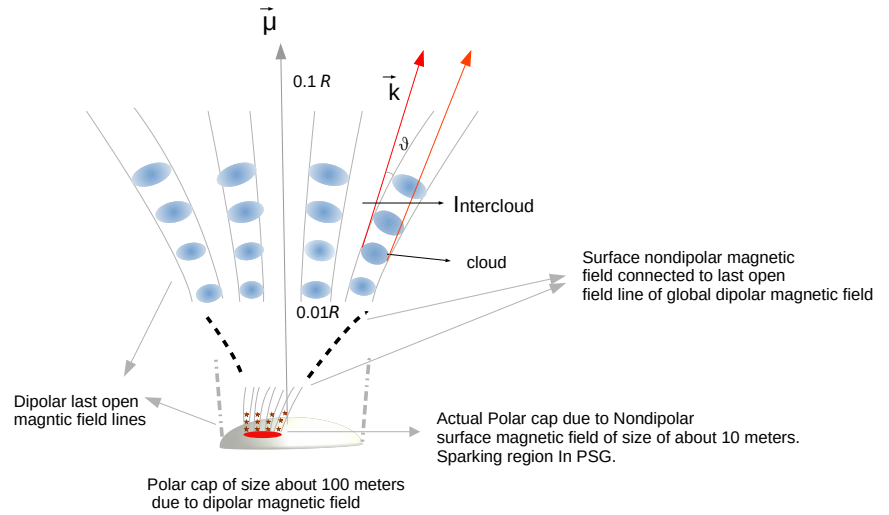


**Figure 6.** The above plot shows a schematic of the PSG model (not to scale). Due to non-dipolar magnetic fields on the surface the actual polar cap (shown as red region) is smaller than the equivalent dipolar case. The PSG exists above the polar cap where non-stationary spark discharges are triggered, shown as red stars in the figure. The open field line region corresponding to the non-dipolar field lines connects to the global dipolar field (shown as dashed black line), and the spark discharges forms plasma clouds with high density regions near the center (blue shaded) and low density region inbetween. CCR is generated in the plasma clouds at about  $\mathcal{R} \sim 0.01$  and the radiation enters the inter-cloud region below  $\mathcal{R} \sim 0.1$ . The inter-cloud regions are the white spaces enclosed within the open magnetic field line region where the density of the particles injected from the adjoining sparks become lower and they are dominated by  ${}^{56}\text{Fe}_{26}$  ions.

The curvature radiation excites the sub-luminal  $t$  and  $lt_1$  modes with polarization directed perpendicular and parallel to dipolar magnetic field line planes, respectively. In the case of curvature radiation emitted by individual particles under vacuum like conditions, the power of the perpendicular component is seven times lower than the parallel component. The two modes propagate independently in the plasma medium, with the  $t$ -mode having vacuum like properties and  $lt_1$ -mode getting ducted along the magnetic field lines. It has been shown that despite the power of the  $t$ -mode of curvature radiation in plasma being suppressed, the emitted intensity is sufficient to account for the observed pulsar luminosity [88]. In order to estimate the rotation of the polarization plane of the modes, the adiabatic walking condition needs to be evaluated, and has the form [59]

$$\left| \frac{1}{k} \frac{\partial}{\partial x} \psi \right| \ll |\Delta N| \quad (2)$$

Here  $N$  is difference between the refractive index of  $t$  and  $lt_1$  mode,  $\Delta N$  is the change in  $N$  as the wave propagates in the medium,  $k$  is the wave vector and  $\psi$  is the linear PPA. In case of curvature radiation from solitons in the radio frequency range, the condition  $v_r \ll v_o$  is satisfied and  $\Delta N \sim 0$ , such that the effects of adiabatic walking is not applicable<sup>2</sup> [82,88]. The waves preserve their polarization direction while escaping from the plasma (also see [92]). The  $lt_1$  mode cannot escape under homogeneous plasma conditions as it gets ducted and eventually undergoes Landau damping. However,  $v_r > v_o$  is possible if the plasma density has large gradients, and then the wave can successfully escape from the plasma. In the PSG model the center of the dense clouds have high pair multiplicity factor,  $\kappa^{sp}$ , while as one moves towards the boundary between adjacent clouds the multiplicity factor,  $\kappa^{isp}$ ,

<sup>2</sup> Note that [59] found adiabatic walking to be important as they were considering an emission mechanism where the radio frequency is close to the characteristic frequency, i.e.  $v_r \approx v_o$ , and  $\Delta N$  has large values.

decreases to orders of unity. This creates a density gradient in the plasma at the inter-cloud boundary through which the  $lt_1$  mode can escape [57,82].

A large number of solitons are produced in each plasma cloud and as the cloud moves along the curved field line the average emission from the cloud passes into the inter-cloud region. The radiation propagates in a rectilinear manner in the inter-cloud region, and due to the curvature of the field lines the angle between  $\vec{k}$  and the tangent to the dipolar magnetic field,  $\vartheta$ , continues to increase. The plasma clouds are expected to give rise to the individual components seen in the average profile, with typical angular width of about  $2^\circ$ . CCR is generated at heights of  $\mathcal{R} \sim 0.01$  where  $\vartheta \sim 0^\circ$  and as the radiation reaches  $\mathcal{R} \sim 0.1$  the angle  $\vartheta$  increases to  $\sim 4^\circ$  which is large enough for the radiation to transfer into the inter-cloud region [57]. Beyond this region  $\vartheta$  does not change with increasing height till  $\mathcal{R} \sim 0.5$ , after which the magnetic field lines bend due to sweepback effects. The  $t$  and  $lt_1$  modes from different plasma clouds enter the inter-cloud region and undergo incoherent addition. This process gives rise to the resultant linear polarization and the associated PPA distribution observed in pulsars. The emission process is stochastic with different clouds having different orientations of the  $\vec{k} \times \vec{B}$  plane, such that averaging will lead to depolarization. From time to time we expect dominant  $t$  or  $lt_1$  modes from strongly magnetized plasma to emerge from the clouds, and the corresponding X- and O-modes will show up as the clear orthogonal PPA tracks observed in Fig. 3. At other times the emergent emission undergoes incoherent mixing of the  $t$ - and  $lt_1$ -modes in various proportions and orientation, resulting in the low levels of linear polarization and scattered PPAs seen in Fig. 4. The plasma clouds can also be associated with the quasi-periodic structures, known as microstructures, observed in single pulses [93,94].

CCR excited in the plasma clouds and subsequently emerging from the inter-cloud region provides a successful mechanism to explain the highly polarized time samples observed in pulsars, but this model still remains largely qualitative. It has also been suggested that in homogeneous plasma the cyclotron damping will affect the plasma modes in the upper magnetosphere, preventing the radiation from escaping [95]. However, the inhomogeneities introduced by the PSG model will reduce the damping effect as the waves propagate in the inter-cloud region. Detailed theoretical studies are still necessary to find the escape condition of  $lt_1$  mode, as well as simulations showing that the incoherent averaging process is able to reproduce the observed polarization characteristics. Our discussions make it clear that propagation effects due to refraction and adiabatic walking have negligible effect in modifying the radiation features.

### 2.3.2. Circular polarization

In early studies of pulsar emission the circular polarization was expected to be a part of the emission process [96–101], although the polarization behaviour is likely to change as the emission propagates within the plasma medium. The circular polarization behaviour of highly polarized time samples from PSR B0329+54 is shown in Fig. 3, where the right window represents the Hammer-Aitoff projection of the Poincaré sphere. The spread of the distribution away from the equatorial plane indicates that almost all polarized time samples are elliptically polarized. This suggests that the linearly polarized  $t$ - and  $lt$ -modes generated in the inner magnetosphere are partially converted into circularly polarized modes as they propagate further in the outer magnetosphere. The polarization behaviour of PSR B0329+54 corresponding to the time samples with lower levels of linear polarization is shown in Fig. 4. The distribution spans a wider azimuthal range on the Poincaré sphere with similar values for both the positive and negative circular polarization. In the entire observing span, shown in Fig. 2, the mean level of absolute circular polarization is about 20%, which is typical for normal pulsars [57]. The models of emission mechanism in pulsars need to explain the observed circular polarization that arises due to propagation effects within the plasma at heights between  $\mathcal{R} \sim 0.01$  and  $\sim 0.1$ .

One of the suggested mechanisms for the appearance of circular polarization is the wave mode coupling that appears due to co-rotation of the magnetosphere [42,59,102,103].

The propagation vector gets tilted with respect to magnetic field line due to co-rotation of the magnetosphere and as it travels a distance  $r_p$ , the adiabatic walking condition adjusts the polarization to generate two independent modes, parallel and perpendicular to the  $\vec{k} \times \vec{B}$  plane. Eventually the adiabatic walking is no longer dominant, resulting in the two modes getting coupled to emerge as elliptically polarized waves. The resultant sense of circular polarization is expected to be constant across the profile, but in reality both sense, i.e. right and left circular polarization are observed across the profile. To address this discrepancy it was suggested that change in the plasma distribution along the open flux tube can bring about the asymmetric nature in the profiles [102]. But as asserted in the previous section, we have ruled out the possibility of adiabatic walking condition to explain the observed high the high linear polarization signals. However, the effects of adiabatic walking and wave coupling on the circular polarization needs further study using realistic model of non-stationary plasma flow.

We consider another possibility where the generation of circular polarization requires breakdown of symmetry in the positive and negative components of the pair plasma. It should be noted that the circular polarization naturally occurs as eigenmodes in a electron plasma. The co-rotational electric field causes the distribution function of electrons and positrons to be slightly different and the presence of ionic species can further break the gyrotropy. In this case the normal modes propagating at small angles with respect to the external magnetic field can be circularly polarized [16,103,104]. The absence of gyrotropy has been used to explain the origin of circular polarization using the PSG model [57]. It is convenient to consider a co-ordinate system [105] with the z-axis along, and introducing  $a_x = E_x/iE_y$ ,  $a_z = E_z/iE_y$ , i.e.  $\vec{E} = E_y(ia_x, 1, ia_z)$ , we can obtain the dispersion relation as:

$$a_x^2 - \Theta a_x - 1 = 0. \quad (3)$$

The solution of equation (3) has the form

$$a_x = \frac{1}{2}\Theta \pm \sqrt{\left(\frac{1}{2}\Theta\right)^2 + 1}. \quad (4)$$

Here  $\Theta$  depends on the plasma parameters. When  $\Theta \ll 1$  then  $a_x \simeq \pm 1$  resulting in circular polarization. In the PSG model the emission enters the ion dominated inter-cloud region at a distance  $\mathcal{R} \gtrsim 0.01$ . In the inter-cloud region, where  $\kappa^{isp} \sim 1$  and  $\mathcal{R} \sim 0.1$ , the radio frequency is higher than the local characteristic frequencies. The wave can propagate rectilinearly and the angle between the wave vector and the local field,  $\vartheta$ , remains constant for large distances, satisfying the conditions  $\sin \vartheta \gg 1/\gamma_s^{isp}$  and  $\sin \vartheta < 1/\gamma_{ion}^{isp}$ . It has been shown [57]  $|\Theta|$  depends on the pulsar parameters as:

$$|\Theta| = \frac{0.087}{\sin^2(\vartheta)} \mathcal{R}^3 \frac{\kappa^{isp}}{(\gamma_s^{isp})^3} \left(\frac{P^5}{\dot{P}_{-15}}\right)^{0.5} \omega. \quad (5)$$

Here  $\gamma_s^{isp}$  is the average Lorentz factor of the electron positron component of the plasma, and  $\omega = 2\pi\nu$  where  $\nu$  is the radio frequency in Hz. Using parameters for PSR B0329+54, and other typical plasma parameters,  $\vartheta \sim 0.07$  radian,  $\gamma_s^{isp} \approx 300$ ,  $\kappa^{isp} = 1$  and  $\nu = 300$  MHz, we estimate  $|\Theta| \sim 0.37$ . This suggests that the above mechanism supports the necessary condition for obtaining circular polarization, i.e.  $|\Theta| \ll 1$ , in PSR B0329+54. The observed circular polarization is an incoherent addition from many different clouds, while the sense of circular polarization depends on the viewing geometry.

### 3. Variation of Spectral Index across the Profile Window

The previous sections have highlighted that the magnetic field has dipolar characteristics at the radio emission heights. The curvature radiation is directly associated with the curvature of field lines. As the LOS traverses across the emission beam, corresponding to

the open dipolar field line region, at any given height the radius of curvature increases from the edge towards the center of the emission beam. The shape of the average profile is determined by the LOS traverse across the emission beam, with distinct physical properties seen in the core component at the center compared to the conal components at the periphery. The CCR from charge bunches predicts a difference in the spectral nature of the flux density between the central core and the peripheral conal components. A proper characterisation of this spectral behaviour provides direct evidence for the emission mechanism in pulsars. Below we summarize the nature of the average emission beam in the pulsar population and the different efforts in constraining the spectral variation across the emission beam.

### 3.1. Classification of Profile Morphology and Nature of Emission Beam

The average profile of each pulsar has unique features and characterised by the number of components that can vary between one and five. The components are classified into two major types, the core component that is usually located at the center of the profile and show large change of the PPA traverse across it with sign changing circular polarization, and the conal components located around the core with relatively shallow PPA slopes and higher levels of linear polarization [35] (also see discussions above). The pulsar profile also shows significant evolution with frequency. The profile widths become wider at lower frequencies due to the effect of radius to frequency mapping, where the lower frequencies originate from higher up the open dipolar field [52]. In addition the number of components in the profile can also change at different frequencies.

The earliest suggestion about the nature of the emission beam was the “hollow cone” model [106,107] where the emission was expected to originate in a narrow cone surrounding the last open field lines, symmetrically around the magnetic axis. However, the hollow cone model was not adequate to explain all observed profile types and has led to the “Core-Cone” model of the emission beam proposed in a series of works [35–38,108], that has the widest applicability in understanding the different profile types. In the core-cone model the emission beam at any observing frequency comprises of a central core region surrounded by two pairs of nested conal rings forming the inner and the outer cones. The profile shape is determined by the pulsar geometry and the distance of the LOS traverse from the magnetic axis. When the LOS cuts the emission beam centrally, close to the magnetic axis, they form the core-cone Triple (T), and core-double cone Multiple (M) profile types. Sometimes one side of the conal component in a T profile is weaker and the profile is classified as  $T_{1/2}$ . The conal Quadruple ( $cQ$ ), conal Triple ( $cT$ ), Double (D) and conal Single ( $S_d$ ) profiles represent the cases of the LOS cuts being progressively away from the magnetic axis missing the central core component and moving towards the edge of the beam. A core Single ( $S_t$ ) represents a central LOS traverse where the conal components are absent. In many cases the  $S_t$  profiles develop conal outriders at higher frequencies, while the  $S_d$  profiles becomes wider and bifurcates at lower frequencies.

In the initial works the core-cone model preserved the hollow-cone structure, with the outer cones and inner cones both bordering the outer field line originating at different heights, while the core was expected to arise from the surface. Subsequent works [109–112] have found that the widths of the core and the conal components have similar distributions with pulsar period and identical lower boundaries. This results confirmed that the core and the conal components originate from similar heights. As a result in the current understanding of the emission beam structure the core component is associated with the central field lines around the dipolar magnetic axis, the inner cones the intermediate field lines between the axis and the open field line boundary, while the outer cones occupy the outermost field lines bordering the boundary. It is expected that the radius of curvature of the magnetic field lines is highest in the core region and progressively decreases towards the inner and outer cones.

Alternative models for the emission beam include the “patchy cone” [113] where the components are expected to arise from similar heights but are distributed randomly within the emission beam. The primary justification for this model comes from the presence of the

“partially conal” profiles where the PPAs are asymmetric and the SG point is shifted towards one edge of the profile. Later studies have shown that in most of these cases the beam shape follows a core-cone structure with one edge of the profile having lower intensity most of the time and only appearing during flaring events in the single pulses [56]. In a few other cases additional components in the form of pre/post cursor emission are seen that are not part of the emission beam [114]. There are also suggestions that the emission beam being a “fan beam” with the components arising from emission along flux tubes [100,115–117]. The fan beam has been used to explain the bifurcated features seen in the profile of certain pulsars. However, its not clear if the characteristics of the different profile morphologies can be explained in this model. Further, the requirement of a tightly packed sparking pattern above the polar cap, that gives rise to subpulse drifting (see discussion below) is also difficult to reconcile with a fan beam without conal symmetry.

There are indications that the emission beam shows evolution with the spin-down energy loss ( $\dot{E}$ ) or characteristic age (see e.g. [118]). The profile classes are not distributed uniformly with  $\dot{E}$ , with  $S_t$  more prevalent in the high  $\dot{E}$  range above  $10^{33}$  erg s<sup>-1</sup>, while the conal profiles corresponding to D and  $S_d$  types are usually seen in pulsars with low  $\dot{E} < 10^{32}$  erg s<sup>-1</sup> [119,120]. The differences in beam shape presented in [55] are subtle, with the fractional polarization between the two subsets being more prominent. Other possibilities include the increase of the number of sparks in high  $\dot{E}$  pulsars with wider open field line region, which form a large number of closely packed components with blurred boundaries between them [121].

### 3.2. Measuring Spectral Variation across the Emission Beam

The coherent radio emission from pulsars have a steep power law spectra between 100 MHz and 10 GHz with spectral index  $\sim -1.8$  [122,123]. The emission beam studies have shown that the central core component in the profiles are associated with the field lines close to the magnetic axis where the radius of curvature is larger, while the conal emission occupies the field lines closer to the boundary of the open field line regions where the magnetic field lines are more curved with relatively smaller values of the radius of curvature. There have been indications that the core components have steeper spectra compared to the cones, e.g. the appearance of conal outriders at higher frequencies in  $S_t$  profile types. However, detailed measurements of the relative spectral indices of the components have not been carried out due to several challenges in estimating the flux density levels of the profile. This primarily arises from the lack of proper instrumental calibration required to scale the measured signal to the appropriate flux densities. In addition, the pulsar signal is also affected by scintillation over timescales varying between several minutes (diffractive scintillation) and extending to several months (refractive scintillation) [124]. As a result the proper estimation of the flux densities require averaging over long timescales which is only available for relatively few pulsars at specific frequencies [125–129]. Other issues affecting flux density estimates, particularly at lower frequencies, involve interstellar scattering [130]. One attempt to measure the spectral index of the different components in the profile by [108] used the Gaussian fitting technique to identify the components. No clear trend of spectral variation between components of the profile was found in this work. However, the Gaussian components were often displaced from actual profile components and made it difficult to have a direct connection between them.

A way around the issue of non-availability of proper flux calibration of the profiles as well as variations due to interstellar scintillation has been devised in our previous works [131], where it was noticed that these effects introduce an unknown but identical multiplicative scaling for all components in the profile. As a result the ratio between the component intensities are expected to be invariant of the measurement conditions and can be used to estimate the relative spectral index of the core with the inner and outer conal components as follows :

$$S_{core} = S_1 v^{\alpha_{core}}; \quad S_{cone} = S_2 v^{\alpha_{cone}}; \quad S_{in} = S_3 v^{\alpha_{in}}; \quad S_{out} = S_4 v^{\alpha_{out}}.$$

$$\begin{aligned}
\left(\frac{S_{core}}{S_{cone}}\right) &= \left(\frac{S_1}{S_2}\right) \nu^{\Delta\alpha_{core/cone}} & \Delta\alpha_{core/cone} &= \alpha_{core} - \alpha_{cone} \\
\left(\frac{S_{core}}{S_{in}}\right) &= \left(\frac{S_1}{S_3}\right) \nu^{\Delta\alpha_{core/in}} & \Delta\alpha_{core/in} &= \alpha_{core} - \alpha_{in} \\
\left(\frac{S_{core}}{S_{out}}\right) &= \left(\frac{S_1}{S_4}\right) \nu^{\Delta\alpha_{core/out}} & \Delta\alpha_{core/out} &= \alpha_{core} - \alpha_{out} \\
\left(\frac{S_{in}}{S_{out}}\right) &= \left(\frac{S_3}{S_4}\right) \nu^{\Delta\alpha_{in/out}} & \Delta\alpha_{in/out} &= \alpha_{in} - \alpha_{out}
\end{aligned} \tag{6}$$

The estimations of the relative spectral index ( $\Delta\alpha_{core/cone}$ ) of the core and the conal components are possible in pulsar profiles with central LOS traverses, such that both the core and conal components are present, i.e. T,  $T_{1/2}$  and M type profiles. In addition, the relative spectral index between the inner and the outer conal pairs ( $\Delta\alpha_{in/out}$ ) can be carried out in M,  $c$ Q and  $c$ T profiles.

Fig. 7 shows frequency evolution of the profile shape of PSR B1821+05 that has a T type profile. The figure shows the measured profiles at six frequency bands between 100 MHz and 5 GHz. At the lowest frequency of 135 MHz only the core component is seen, while the conal components are too weak to be detected. With increasing frequency the relative intensity of the conal components increases with respect to the core and the cones dominate the profile at frequencies above 1 GHz. Fig. 8 shows the spectral plot of the relative intensities between the core and the cone ( $S_{core}/S_{cone}$ ) between 100 MHz and 10 GHz, with the estimated spectral index  $\Delta\alpha_{core/cone} = -1.55 \pm 0.10$  (see line in Fig. 8), demonstrating the core to have a much steeper spectral index compared to the conal emission. At the lowest frequency range the conal components are not visible in the profile and hence the relative intensities cannot be measured. The core emission at 4.8 GHz merges with the trailing conal component (see Fig. 7, bottom right panel), leading to imprecise measurements. As a result at the highest frequency the relative intensities deviate from the linear spectral behaviour.



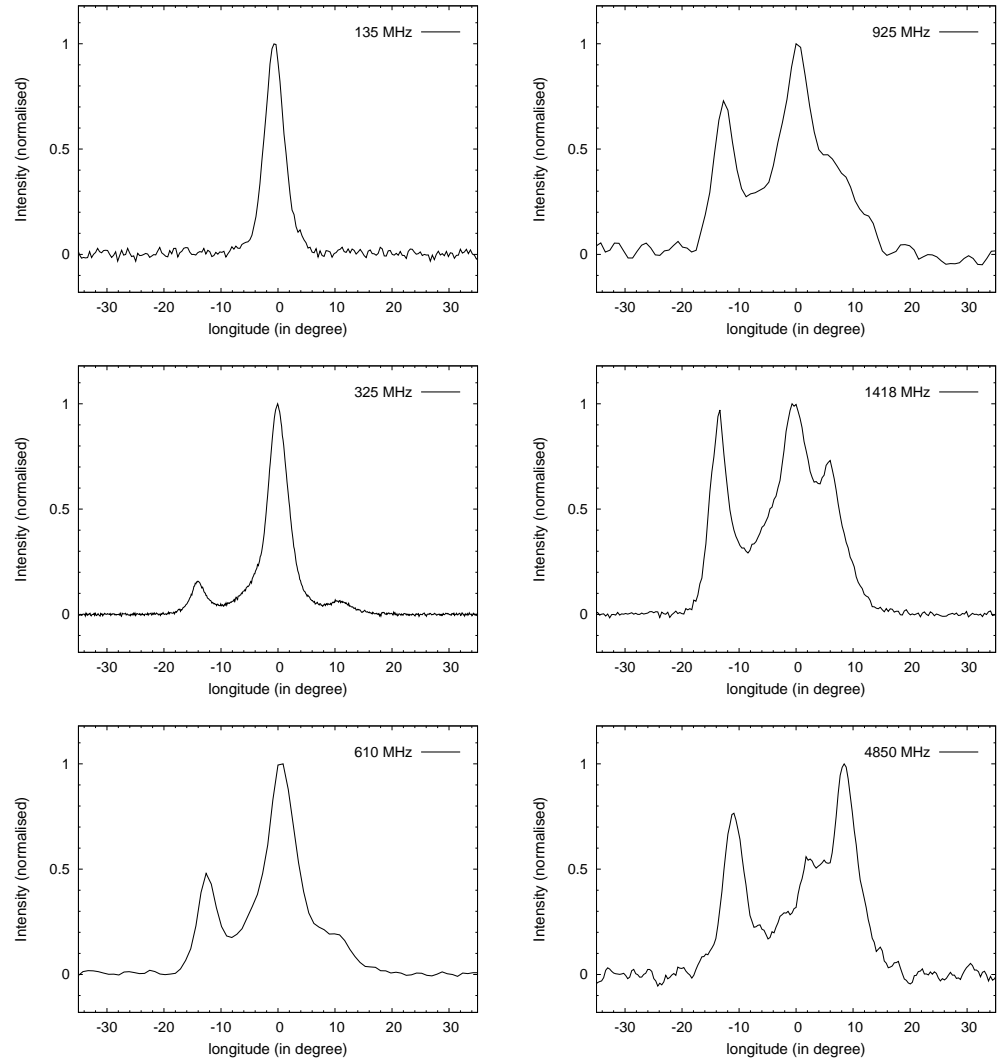


**Figure 7.** The Figure shows the T type average profile of PSR B1821+05 at 6 different frequencies at 135 MHz (top left), 325 MHz (middle left), 610 MHz (bottom left), 925 MHz (top right), 1408 MHz (middle right) and 4850 MHz (bottom right). The core component in the center of the profile is stronger at the lower frequencies and becomes weaker compared to the surrounding cones with increasing frequency.

Similar studies have been carried out in around 50 pulsars having both core and conal components in their profiles [131] and in all cases the core component have a steeper spectra than the cones, with  $\Delta\alpha_{core/cone}$  varying between -0.4 and -2.0. The radius of curvature of the magnetic field lines are expected to change between the core and the conal components and the only known emission mechanism that has direct dependence on the radius of curvature of the field lines is CCR from charge bunches. As a result the observational result of the core having a steeper spectral index than the conal components within the pulsar profile strongly favours the radio emission mechanism in pulsars to be CCR.

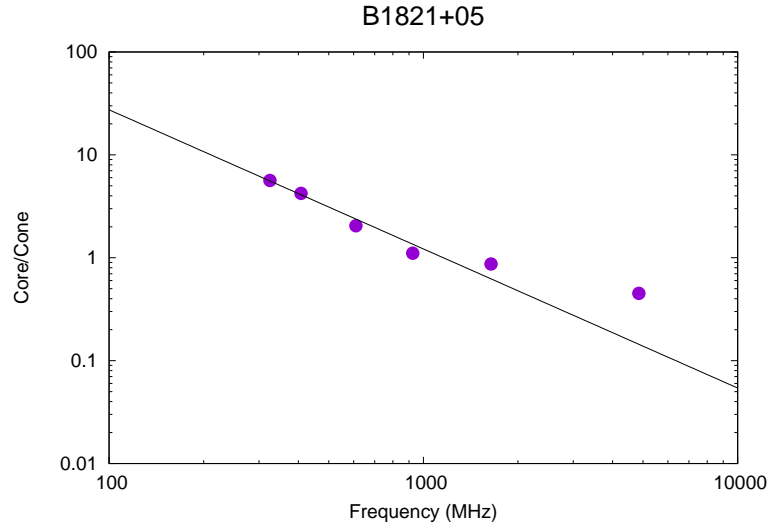


**Figure 8.** The Figure shows the frequency evolution of the relative intensities of the core and the conal components ( $S_{core}/S_{cone}$ ) of PSR B1821+05 between 100 MHz and 10 GHz. **The power law fit to the relative spectral index shown by solid black line has spectral index of  $-1.55 \pm 0.1$ .**

#### 4. Subpulse Drifting : Window into Inner Acceleration Region

The CCR from charge bunches needs the presence of a multi-component electron-positron plasma in the form of plasma clouds, separated by less dense regions filled with positively charged ions, and requires a non-stationary plasma flow. In this section we briefly summarize our understanding of the plasma generation process in pulsars and its observational signature in the form of subpulse drifting.

The plasma is expected to be generated in an inner acceleration region (IAR) above the polar cap extending to heights of around 10-100 m. In one of the earlier studies by [12] the IAR was considered to be a Vacuum Gap (IVG). The IVG is characterised by very high magnetic fields ( $\sim 10^{13}$  G) as well as large electric potential difference ( $10^{12}$  V) along the magnetic field. Under these extreme conditions regular breakdown of the gap in the form of spark discharges is expected. This mechanism of plasma generation is possible in pulsars where  $\vec{\Omega} \cdot \vec{B} < 0$  (here  $\Omega = 2\pi/P$  is the angular velocity of the neutron star), such that positively charged particles are accelerated away from the stellar surface while the negatively charged particles are accelerated towards the surface. In the IVG the electron-positron pairs are produced from ambient  $\gamma$ -ray photons and accelerated to high energies with Lorentz factor  $\gamma_b \sim 10^6$  [10]. The positrons are accelerated away from the gap and produce additional  $\gamma$ -ray photons due to curvature radiation or inverse Compton scattering as they propagate along the curved magnetic field lines. These additional  $\gamma$ -ray photons generate further pairs resulting in a cascading effect. Effective break down of the gap requires the magnetic field to be highly curved and non-dipolar in nature such that high energy  $\gamma$ -ray photons can be produced. In this process a primary plasma beam comprising of high energetic positrons is formed.

When the charge density in the IVG equals the Golreich-Julian density,  $\rho_{GJ} = \Omega B / 2\pi c$  [9], the electric potential difference along the magnetic field is fully screened and pair production is halted. The potential difference reappears once the plasma escapes the gap due to inertial motion and the next sparking event is triggered forming the non-stationary plasma flow. The primary particles continue to produce additional pairs outside the IAR to form clouds of secondary pair plasma that are considerably less energetic, with Lorentz factors,  $\gamma_s^{sp}$  between 100 and 1000, and has high multiplicity,  $\kappa^{sp} \sim 10^4$  [10]. The CCR develops in these spark associated secondary plasma clouds that stream outwards along the open magnetic field line region.

Subsequent works have revealed several limitations of the IVG model of IAR. The back-flowing electrons produced during sparking are expected to heat the surface to temperatures of  $10^6$  K, that are near the critical level for ions ( $T_i$ ) to be emitted freely from

the surface and screen the potential difference along the magnetic field [132,133]. In a purely vacuum gap there is no mechanism to constrain the lateral size of the sparks as there is unscreened potential difference in the boundary between two adjacent sparks. As a result the primary particles cannot be confined to any specific location within the IVG, but likely scatter in the direction opposite to principal normal to the curvature of the local magnetic field lines [132].

In order to address the heating of the surface due to back-flowing electrons during sparking an updated model of the IAR has been proposed. It has been suggested that the IAR is not a complete vacuum but has a steady supply of positively charged ions from the surface and forms a Partially Screened Gap (PSG) [91]. The potential difference along the gap is reduced by a screening factor  $\eta = 1 - \rho_i / \rho_{GJ}$ , where  $\rho_i$  is the average density of ions in the gap. In a PSG the sparking process is primarily a mechanism to regulate the surface temperature around  $T_i$  of ionic free flow. When the surface temperature ( $T_S$ ) is close to  $T_i$  there is free flow of ions from the surface and the potential difference along the IAR is screened. As the surface cools down and  $T_S < T_i$ , the supply of ions from the surface decreases such that the density goes below  $\rho_{GJ}$  and the potential difference appears in the IAR. This starts the sparking process and the primary plasma is produced along with the back-flowing electrons that once again heat the surface to critical level thereby terminating the spark. The typical timescale for each spark to develop and empty the IAR is around 30  $\mu$ seconds, while the surface cools rapidly once the sparking stops with typical cooling time of 30 nseconds.

When a spark starts at a location within IAR, it also spreads out across the field lines till enough particles are produced to heat the surface and screen the potential difference along the magnetic field. As a result the lateral size of the sparks ( $h_{\perp}$ ) is regulated by the energy that needs to be deposited on the surface for the thermal regulation process. The PSG is the only known mechanism for confining sparks in the IAR, where the sparking location is determined by the surface temperature profile. The sparks are formed in a tightly packed manner for effective thermal regulation of the surface. The peak density is near the center of the spark and the density gradually decreases towards the edge, with the boundary between two sparks dominated by the ions emitted from the surface. The primary plasma produced in the sparks leave the IAR and they give rise to the columns of secondary plasma clouds. The inter-cloud regions correspond to the boundary between sparks, and are dominated by the positively charged ions. For a typical normal pulsar the Lorentz factor of the secondary pair plasma is  $\gamma_s^{sp} = \gamma_s^{isp} \sim 100$  and the Lorentz factor of the ion component  $\gamma_{ion}^{sp} \sim 10^3$ , where superscript "sp" and "isp" stands for the spark and interspark region. The multiplicity  $\kappa^{sp} \sim 10^4$  at the center of the spark which gradually becomes  $\kappa^{isp} \sim 1$  in the interspark region. The Lorentz factor of the ion in the interspark region is  $\gamma_{ion}^{isp} \sim 10$ . In terms of pulsar parameters  $P$  and  $\dot{P}_{15}$  and  $\mathcal{R}$ , the plasma frequency of the pair plasma is  $\omega_p = 6.4151 \times 10^4 \kappa^{0.5} \mathcal{R}^{-1.5} P^{-1.75} \dot{P}_{15}^{0.25}$  and the ion plasma frequency is  $\omega_{p,ion} = 1.02 \times 10^3 \mathcal{R}^{-1.5} P^{-1.75} \dot{P}_{15}^{0.25}$ , where ion  ${}^{56}\text{Fe}_{26}$  species is used (see [57] for these estimates).

When the pulsar magnetosphere is filled up with  $\rho_{GJ}$ , the plasma co-rotates with the star due to  $\vec{E} \times \vec{B}$  drift. During sparking the plasma density in the IAR is less than  $\rho_{GJ}$  and plasma no longer co-rotates with the star. The sparks during their lifetimes lag behind the rotation of the star [134], and the location of maximum heating/cooling shifts opposite to the direction of rotation as the spark develops. Once the plasma empties and the surface cools down the next spark is formed slightly shifted in the direction opposite to rotation. This lack of co-rotation is imprinted in the plasma clouds as they move along the open field line region and emit radio waves. The effect is seen in the single pulse behaviour of certain pulsars as the phenomenon of subpulse drifting [135–137]. The subpulse drifting is intricately connected to the conditions in the IAR, like the potential difference along the magnetic field, the nature of non-dipolar magnetic fields, the surface conditions, etc. We describe below the measurement of the drifting behaviour in pulsars and how these results can be used to obtain observational evidence for the presence of non-dipolar fields

above the stellar surface and for the IAR to be a PSG. This in turn puts the presence of plasma clouds in the open field line region, the presence of multi-component plasma, and the dominance of  $^{56}\text{Fe}_{26}$  ions between plasma clouds, on a firm observational footing.

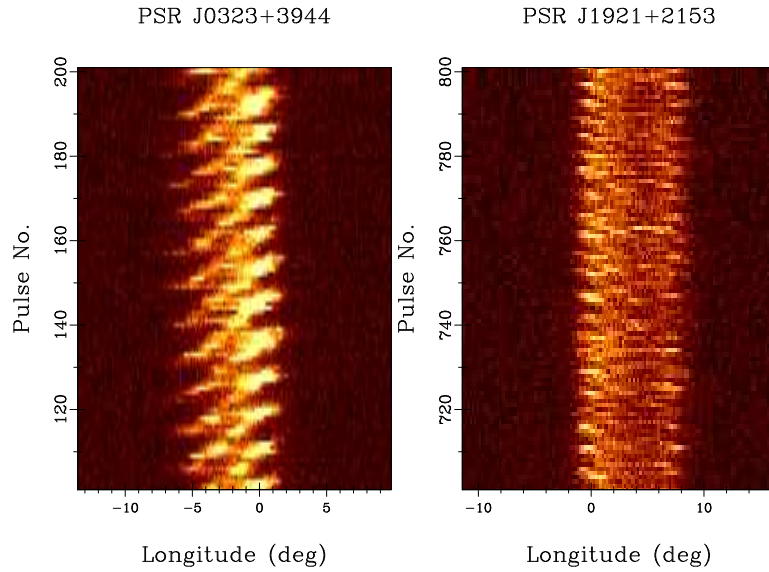


**Figure 9.** The Figure shows single pulse stack of PSR J0323+3944 (or PSR B0320+39) at 333 MHz (left panel) and PSR J1921+2153 (or PSR B1919+21) at 610 MHz (right panel), where the subpulse drifting phenomenon is clearly observed. The data is obtained from the GMRT and for details see [119].

#### 4.1. Drift Phase Variations : Evidence of Non-dipolar Magnetic Field

The single pulse emission in pulsars comprise of one or more constituents that are called subpulses. In certain cases the subpulses show systematic periodic shifts and the phenomenon is called subpulse drifting which was first discovered by [138]. The drifting behaviour is best visualized when the single pulses are represented in the form of a pulse stack which is a two dimensional plot with the rotation longitude along the x-axis and the pulse number in the y-axis. Two examples of subpulse drifting is shown in Fig. 9. The nature of the drifting behaviour is associated with the profile morphology and LOS geometry [119]. The pulsars with large shift of the subpulses across the emission window have conal profiles of  $S_d$  and  $D$  types (see previous section). On the contrary the M type profile usually have very little shift in position of the subpulses but periodic modulation of intensity in their conal components. The central core component in these profiles do not show any drift behaviour. The intermediate LOS profiles like  $cT$  and  $cQ$  show complex drift behaviour with reversals in drift direction, also known as bi-drifting, between different components of the profile in a few cases. The drifting behaviour is measured using the fourier transformation technique, like the Longitude Resolve Fluctuation Spectra (LRFS) [139], where Fourier transforms are carried out along each longitude range of the pulse stack for a fixed number of pulses. The drifting periodicity ( $P_3$ ), that represents the time interval between subpulses repeating at any longitude, is seen as a peak frequency in the LRFS. The phase variations corresponding to the peak frequency shows the track of the subpulses across the profile window (see Fig. 10).

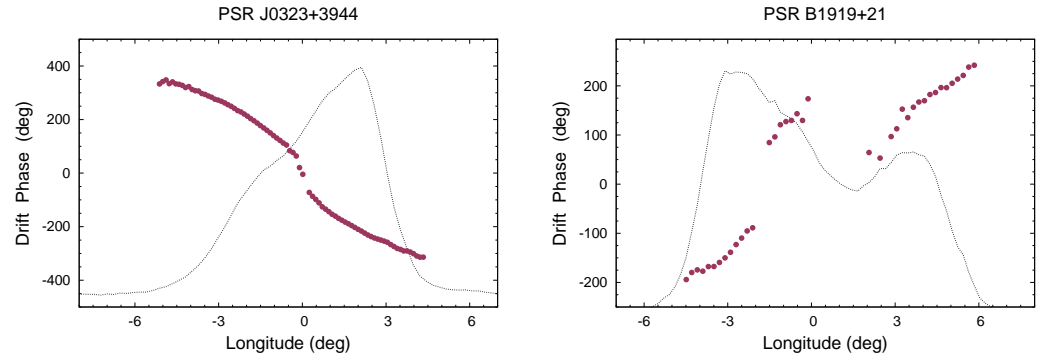


**Figure 10.** The Figure shows the phase variation of the drifting subpulses across the profile of PSR J0323+3944 at 333 MHz (left panel) and PSR B1919+21 at 610 MHz (right panel).

As discussed earlier the sparks in a PSG are formed in tightly packed configuration and lag behind the rotation motion of the star [134]. The subsequent sparks are formed slightly shifted in the direction opposite to the rotation of the star. In addition, the well defined polar cap boundary separating the open and closed field line region of the magnetosphere constrains the later sparks to be formed along the boundary. Hence, the two dimensional sparking pattern in the IAR evolves with time along two different directions, in a clockwise and counterclockwise manner in the two halves of the polar cap. In the center of the IAR the sparks are formed at regular intervals in roughly the same location since there is no space for shifting. The central sparks makes up the core component in the profile that does not show any drifting behaviour.

The drifting periodicity as well as the phase variations can be associated with the sparking process in the IAR. The drifting periodicity measures the electric potential difference and particularly the screening factor,  $\eta$ , of PSG and will be discussed in the next subsection. The phase variations across the profile traces the evolutionary track of the sparking pattern along the projection of the LOS (see Fig. 11, left panel). As a result the phase behaviour has information regarding the shape of the polar cap which is determined by the nature of the surface magnetic field. In case of purely dipolar field the phase variations are expected to be mostly linear with small deviations near the edge of the inner and outer cones. The expected phase variations of drifting for an intermediate LOS cut located midway between the magnetic axis and the polar cap edge has been simulated and shown in Fig. 11 (see [134] for details). The phase behaviour is mostly linear across the entire profile with small deviations at the crossing between the inner and the outer cones, and near the edges. The measured phase variations for two pulsars PSR J0323+3944 (left panel) and PSR B1919+21 (right panel) is shown in Fig. 10. The phases show larger deviation from linearity and significant jumps between components, confirming that the surface magnetic fields in pulsars are non-dipolar in nature. The direction of the slope of the phase changes are reversed in these two pulsars and has a degenerate origin, either due to the drifting periodicity being aliased or the local magnetic field on the surface being highly twisted [134].

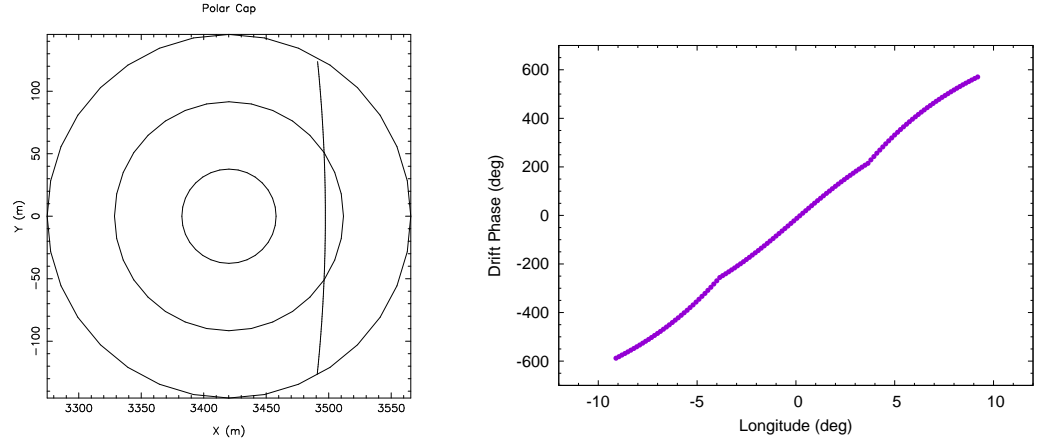


**Figure 11.** The Figure shows the modelled phase variations of subpulse drifting from a polar cap with dipolar magnetic field. The left panel shows the LOS traverse across the polar cap, where the three concentric rings demarcate the core, inner and outer conal regions. The LOS traverse cuts across the polar cap about halfway between the axis and the open field line boundary. The right panel shows the simulated phase variations of the drifting subpulses for this configuration.

#### 4.2. Dependence of Drift Periodicity with $\dot{E}$ : Evidence of Partially Screened Gap

The drifting periodicity is the time taken by subsequent sparks to lag behind the extent of the spark diameter, such that the subpulse peaks appear at the same longitude in the emission window. The speed at which the sparking pattern shifts in the gap is  $v_{sp} = \eta(E/B)c$ , and the repetition time is estimated as  $P_3 = h_{\perp}/v_{sp} = 1/2\pi\eta \cos \alpha_l$  [134], here  $\alpha_l$  is the angle of the local magnetic field with the rotation axis.

The total energy outflow from the PSG ( $L_{PSG}$ ) due to the outflowing plasma can be estimated as [137]:

$$L_{PSG} \simeq \gamma_b m_e c^3 \eta n_{GJ} A_{pc}. \quad (7)$$

Here,  $n_{GJ} = \rho_{GJ}/e$ , and  $A_{pc}$  is the area of the polar cap. The quantity  $n_{GJ} A_{pc}$  is invariant of the nature of the surface fields due to conservation of magnetic flux and can be estimated as

$$n_{GJ} A_{pc} = 2 \times 10^{19} \cos \alpha_l (\dot{P}_{-15}/P^3)^{0.5}, \quad (8)$$

Additionally,  $\dot{E}$  is also obtained from  $P$  and  $\dot{P}_{-15}$  in the form  $\dot{E} = 4 \times 10^{31} (\dot{P}_{-15}/P^3) \text{ erg s}^{-1}$ . The ratio between  $L_{PSG}$  and  $\dot{E}$  has the form:

$$\zeta = \frac{L_{PSG}}{\dot{E}} \simeq 1.2 \times 10^{-8} \eta \gamma_b \cos \alpha_l \left( \frac{\dot{E}}{\dot{E}_1} \right)^{-0.5}, \quad (9)$$

Here,  $\dot{E}_1 = 4 \times 10^{31} \text{ erg s}^{-1}$ . The PSG model provides a direct connection between two independent measurable from pulsars,  $P_3$  and  $\dot{E}$  which has the form

$$P_3 \simeq 2 \times 10^{-9} \left( \frac{\gamma_p}{\zeta} \right) \left( \frac{\dot{E}}{\dot{E}_1} \right)^{-0.5}, \quad (10)$$

i.e. we obtain a dependence  $P_3 \propto \dot{E}^{-0.5}$  between the two quantities.

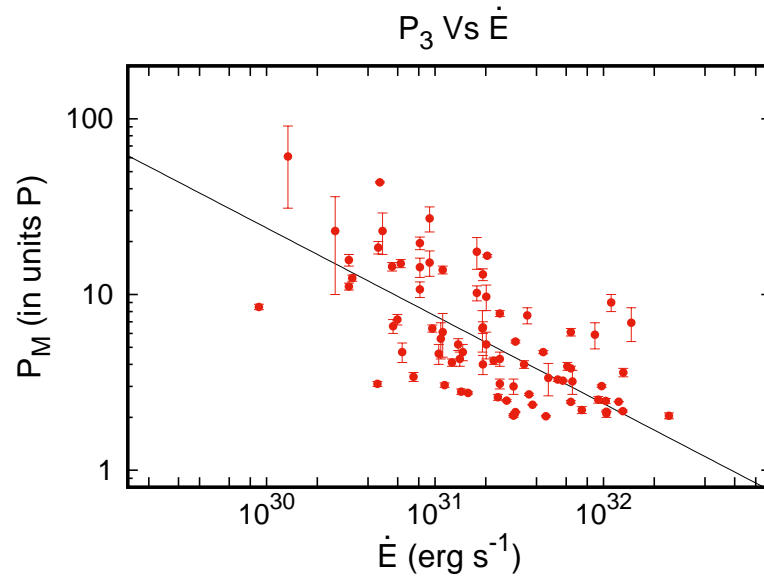


**Figure 12.** The Figure shows the distribution of drifting periodicity ( $P_3$ ) with the spin-down energy loss ( $\dot{E}$ ). The black line shows the expected  $P_3 \propto \dot{E}^{-0.5}$  dependence from the Partially Screened Gap model of the Inner Acceleration Region.

The distribution of  $P_3$  with  $\dot{E}$  has been estimated in a number of works [119,137,140] and reproduced in Fig. 12, with additional  $P_3$  measurements from recent works added to the figure [141–148]. The drifting behaviour is often conflated with the periodic nulling and periodic modulation features seen in pulsars [149], that have quasi-periodic variation unrelated to the sparking process in the IAR [140]. We have restricted the  $P_3$  in Fig. 12 to cases with clear indications of drifting in the single pulses. Although, there is a prospect of aliasing associated with the  $P_3$  measurements, where any intrinsic  $P_3 < 2P$  is seen as a higher periodic feature  $P_3^a = 1/(1 - 1/P_3) > 2P$ , the general trend of the anti-correlation between  $P_3$  and  $\dot{E}$  is evident in Fig. 12. Additional support for the presence of such dependence is also seen in the grouping of periodicities at the alias boundary  $2P$  near  $\dot{E} = 10^{32}$  erg s $^{-1}$ . Some pulsars above this range shows an increase in their  $P_3$  suggesting an aliased measurement, which will be expected from the anti-correlation. The figure also shows the  $\dot{E}^{-0.5}$  dependence (black line) of the PSG model which is consistent with the distribution. The scatter in the plot is also explained in this model due to the dependence on parameters like  $\gamma_p$  and  $\zeta$ , that are likely to vary between different pulsars. The presence of anti-correlation between two independent measurables,  $P_3$  and  $\dot{E}$ , provide strong observational justification for the IAR to be a PSG.

## 5. Summary

The identification of highly linearly polarized signals following the RVM in conjunction with the findings that pulsar radio emission from normal pulsars detach from regions below  $0.1\mathcal{R}$  strongly suggest that CCR is the radio emission mechanism in pulsars. The OPMs indicate that the linearly polarized orthogonal modes are excited in strongly magnetized pair plasma that can reach the observer as X- and O-mode. The observed circular polarization suggests the presence of an ion component in the plasma. The multiple-component average profiles, the single pulse quasi-periodic structure and subpulse drifting requires non-stationary plasma flow and strong non-dipolar surface magnetic fields. Hence, these observational evidences provide the framework of the necessary conditions for CCR to develop.

CCR from charge bunches has been considered as a plausible candidate for radio emission mechanism from the beginning of pulsar research. However, there are still some questions raised regarding a suitable theory that can justify the existence of a stable charge bunches in pulsar plasma. Alternate emission mechanisms such as maser mechanism has

also been suggested for the radio emission in pulsars, however these theories do not have adequate observational support. Studies addressing the issue of charge bunch formation on the other hand resulted in identifying the existence of stable relativistic charged solitons in the pulsar plasma [15,90,150]. These studies are performed in the one dimensional approximation, whereas realistically stable charge bunch formation needs to be established in two or three dimensions. The overwhelming observational evidence for CCR in pulsars strongly motivates theoretical research in these directions. In the accompanying article by Melikidze, Mitra & Basu the development and current state of the theory of charge bunch formation in pulsar plasma is reviewed.

The enhanced sensitivity of radio Telescopes in conjunction with improved data analysis methods in recent years have revealed a plethora of interesting new phenomena from pulsars. While we are fairly confident that the radio emission mechanism from normal pulsars is CCR, there are other issues that still remain unclear. Below we list some of these key problems associated with the pulsar activity.

1. The origin and shape of the pulsar emission beam and its evolution with  $\dot{E}$  (see e.g. [118]).
2. The physical origin of the evolution of average profile width, component width and component separation with frequency, and their dependence on the emission height (see accompanying paper Melikidze, Mitra & Basu, also see e.g. [52]).
3. The origin of inter-pulse emission and the post/pre-cursor and off-pulse emission outside the main pulse window (e.g. [114,151–153]).
4. The complete absence of subpulse drifting in pulsars with  $\dot{E} > 5 \times 10^{32} \text{ erg s}^{-1}$  and also in around 50% of the population below this limit (e.g. [119,136,149]).
5. What causes the phenomenon of mode (or state) changing and to explain the observed correlation/anticorrelation between radio and X-ray intensities during mode changing ([154]. Also what causes the weak emission detected in the null state of pulsars ([155,156]).
6. How does pulsar signals escape the pulsar magnetosphere? (see e.g. [82,92])
7. It is worth mentioning that, unlike normal pulsars, in millisecond pulsars the location of the radio emission region has not been constrained and as a result the coherent radio emission mechanism is still unknown (see e.g. [157–159]) ?
8. What is the origin of radio emission from Magnetars (see e.g. [160])?

The above list is not exhaustive but gives a flavour of the exciting scientific problems that can be explored in the future.

**Funding:** D.M. acknowledges the support of the Department of Atomic Energy, Government of India, under project No. 12-R&DTFR-5.02-0700. This work was supported by the grant 2020/37/B/ST9/02215 of the National Science Centre, Poland.

**Acknowledgments:** We thank the staff of the GMRT, who made these observations possible. D.M. acknowledges the support of the Department of Atomic Energy, Government of India, under project No. 12-R&DTFR-5.02-0700. This work was supported by the grant 2020/37/B/ST9/02215 of the National Science Centre, Poland.

**Conflicts of Interest:** The authors declare no conflict of interest.

### Abbreviations

The following abbreviations are used in this manuscript:



CCR	Coherent Curvature Radiation
GMRT	Giant Metrewave Radio Telescope
IAR	Inner Acceleration Region
IVG	Inner Vacuum Gap
LOS	Line Of Sight
LRFS	Longitude Resolve Fluctuation Spectra
<i>lt</i> -mode	Longitudinal Transverse mode
OPM	Orthogonal Polarization Mode
O-mode	Ordinary mode
PPA	Polarization Position Angle
PSG	Partially Screened Gap
RVM	Rotating Vector Model
SG	Steepest Gradient
<i>t</i> -mode	Transverse mode
u-GMRT	upgraded Giant Metrewave Radio Telescope
X-mode	Extraordinary mode

## References

- Hewish, A.; Bell, S.J.; Pilkington, J.D.H.; Scott, P.F.; Collins, R.A. Observation of a Rapidly Pulsating Radio Source. *Nature* **1968**, *217*, 709–713. <https://doi.org/10.1038/217709a0>.
- Gold, T. Rotating Neutron Stars and the Nature of Pulsars. *Nature* **1969**, *221*, 25–27. <https://doi.org/10.1038/221025a0>.
- Large, M.I.; Vaughan, A.E.; Wielebinski, R. Pulsar Search at the Molonglo Radio Observatory. *Nature* **1968**, *220*, 753–756. <https://doi.org/10.1038/220753a0>.
- Staelin, D.H.; Reifenstein, Edward C., I. Pulsating Radio Sources near the Crab Nebula. *Science* **1968**, *162*, 1481–1483. <https://doi.org/10.1126/science.162.3861.1481>.
- Comella, J.M.; Craft, H.D.; Lovelace, R.V.E.; Sutton, J.M. Crab Nebula Pulsar NP 0532. *Nature* **1969**, *221*, 453–454. <https://doi.org/10.1038/221453a0>.
- Cocke, W.J.; Disney, M.J.; Taylor, D.J. Discovery of Optical Signals from Pulsar NP 0532. *Nature* **1969**, *221*, 525–527. <https://doi.org/10.1038/221525a0>.
- Lynds, R.; Maran, S.P.; Trumbo, D.E. Optical Identification and Observations of the Pulsar NP 0532. *Astrophysical Journal, Letters* **1969**, *155*, L121. <https://doi.org/10.1086/180316>.
- Ginzburg, V.L.; Zheleznyakov, V.V.; Zaitsev, V.V. Coherent Mechanisms of Radio Emission and Magnetic Models of Pulsars. *Astrophysics and Space Science* **1969**, *4*, 464–504. <https://doi.org/10.1007/BF00651351>.
- Goldreich, P.; Julian, W.H. Pulsar Electrodynamics. *Astrophysical Journal* **1969**, *157*, 869. <https://doi.org/10.1086/150119>.
- Sturrock, P.A. A Model of Pulsars. *Astrophysical Journal* **1971**, *164*, 529. <https://doi.org/10.1086/150865>.
- Ginzburg, V.L.; Zhelezniakov, V.V. On the pulsar emission mechanisms. *Annual Review of Astron and Astrophysics* **1975**, *13*, 511–535. <https://doi.org/10.1146/annurev.aa.13.090175.002455>.
- Ruderman, M.A.; Sutherland, P.G. Theory of pulsars: polar gaps, sparks, and coherent microwave radiation. *Astrophysical Journal* **1975**, *196*, 51–72. <https://doi.org/10.1086/153393>.
- Qiao, G. A mechanism for core emission of pulsars. *Vistas in Astronomy* **1988**, *31*, 393–397. [https://doi.org/10.1016/0083-6656\(88\)90234-6](https://doi.org/10.1016/0083-6656(88)90234-6).
- Qiao, G.J. Inverse Compton scattering (ICS) plays an important role in pulsar emission. In Proceedings of the High Energy Astrophysics, 1988, p. 88.
- Melikidze, G.I.; Gil, J.A.; Pataraya, A.D. The Spark-associated Soliton Model for Pulsar Radio Emission. *Astrophysical Journal* **2000**, *544*, 1081–1096, [arXiv:astro-ph/0002458]. <https://doi.org/10.1086/317220>.
- Kazbegi, A.Z.; Machabeli, G.Z.; Melikidze, G.I. On the circular polarization in pulsar emission. *Monthly Notices of the RAS* **1991**, *253*, 377. <https://doi.org/10.1093/mnras/253.3.377>.
- Melrose, D.B. Coherent Radio Emission from Pulsars. *Philosophical Transactions of the Royal Society of London Series A* **1992**, *341*, 105–115. <https://doi.org/10.1098/rsta.1992.0087>.
- Melrose, D.B. The models for radio emission from pulsars - The outstanding issues. *Journal of Astrophysics and Astronomy* **1995**, *16*, 137–164. <https://doi.org/10.1007/BF02714830>.
- Melrose, D.B.; Rafat, M.Z.; Mastrano, A. Pulsar radio emission mechanisms: a critique. *Monthly Notices of the RAS* **2021**, *500*, 4530–4548, [arXiv:astro-ph.HE/2006.15243]. <https://doi.org/10.1093/mnras/staa3324>.
- Hardee, P.E.; Rose, W.K. Wave production in an ultrarelativistic electron-positron plasma. *Astrophysical Journal* **1978**, *219*, 274–287. <https://doi.org/10.1086/155774>.
- Arons, J.; Barnard, J.J. Wave Propagation in Pulsar Magnetospheres: Dispersion Relations and Normal Modes of Plasmas in Superstrong Magnetic Fields. *Astrophysical Journal* **1986**, *302*, 120. <https://doi.org/10.1086/163978>.
- Shpakidze, D.; Machabeli, G.; Melikidze, G.; Khechinashvili, D. Quasilinear theory of Cherenkov-drift instability. *Physical Review E* **2003**, *67*, 026407. <https://doi.org/10.1103/PhysRevE.67.026407>.

23. Radhakrishnan, V.; Cooke, D.J. Magnetic Poles and the Polarization Structure of Pulsar Radiation. *Astrophysics Letters* **1969**, *3*, 225.
24. Wampler, E.J.; Scargle, J.D.; Miller, J.S. Optical Observations of the Crab Nebula Pulsar. *Astrophysical Journal, Letters* **1969**, *157*, L1. <https://doi.org/10.1086/180372>.
25. Böhm-Vitense, E. The Pulsar NP 0532 and the Implications of the Oblique-Rotator Hypothesis. *Astrophysical Journal, Letters* **1969**, *156*, L131. <https://doi.org/10.1086/180364>.
26. Morris, D.; Berge, G.L. Measurements of the polarization and angular extent of the decimetric radiation of Jupiter. *Astrophysical Journal* **1962**, *136*, 276–282. <https://doi.org/10.1086/147372>.
27. du Plessis, L.; Wadiasingh, Z.; Venter, C.; Harding, A.K. Constraining the Emission Geometry and Mass of the White Dwarf Pulsar AR Sco Using the Rotating Vector Model. *Astrophysical Journal* **2019**, *887*, 44, [arXiv:astro-ph.HE/1910.07401]. <https://doi.org/10.3847/1538-4357/ab4e19>.
28. Radhakrishnan, V. Fifteen Months of Pulsar Astronomy. *Publications of the Astron. Soc. of Australia* **1969**, *1*, 254–263. <https://doi.org/10.1017/S1323358000011826>.
29. Lerche, I. On the Motion of Current Sheets, and the Radio, Optical, and X-Ray Emission from Pulsars. II. Pulse Structure, Polarization, Time-Varying Features, and Tight-Beam Emission. *Astrophysical Journal* **1970**, *160*, 1003. <https://doi.org/10.1086/150488>.
30. Manchester, R.N.; Taylor, J.H.; Huguenin, G.R. Observations of pulsar radio emission. II. Polarization of individual pulses. *Astrophysical Journal* **1975**, *196*, 83–102. <https://doi.org/10.1086/153395>.
31. Manchester, R.N. Orthogonal Polarization in Pulsar Radio Emission. *Publications of the Astron. Soc. of Australia* **1975**, *2*, 334–336. <https://doi.org/10.1017/S132335800001417X>.
32. Backer, D.C.; Rankin, J.M.; Campbell, D.B. Orthogonal mode emission in geometric models of pulsar polarisation. *Nature* **1976**, *263*, 202–207. <https://doi.org/10.1038/263202a0>.
33. Cocke, W.J.; Pacholczyk, A.G. Theory of the polarization of pulsar radio radiation. *Astrophysical Journal, Letters* **1976**, *204*, L13–L15. <https://doi.org/10.1086/182044>.
34. Melrose, D.B.; Stoneham, R.J. The natural wave modes in a pulsar magnetosphere. *Publications of the Astron. Soc. of Australia* **1977**, *3*, 120–122. <https://doi.org/10.1017/S1323358000015010>.
35. Rankin, J.M. Toward an empirical theory of pulsar emission. I. Morphological taxonomy. *Astrophysical Journal* **1983**, *274*, 333–358. <https://doi.org/10.1086/161450>.
36. Rankin, J.M. Toward an Empirical Theory of Pulsar Emission. IV. Geometry of the Core Emission Region. *Astrophysical Journal* **1990**, *352*, 247. <https://doi.org/10.1086/168530>.
37. Rankin, J.M. Toward an Empirical Theory of Pulsar Emission. VI. The Geometry of the Conal Emission Region. *Astrophysical Journal* **1993**, *405*, 285. <https://doi.org/10.1086/172361>.
38. Rankin, J.M. Toward an Empirical Theory of Pulsar Emission. VI. The Geometry of the Conal Emission Region: Appendix and Tables. *Astrophysical Journal, Supplement* **1993**, *85*, 145. <https://doi.org/10.1086/191758>.
39. Ferguson, D.C. The Optical Polarization of the Crab Nebula Pulsar. I. A Relativistic Vector Model. *Astrophysical Journal* **1973**, *183*, 977–986. <https://doi.org/10.1086/152284>.
40. Ferguson, D.C. The generalized single-vector polarization model for pulsars. I. Theory. *Astrophysical Journal* **1976**, *205*, 247–260. <https://doi.org/10.1086/154270>.
41. Shitov, Y.P. Pulsar Radio Polarization and the Magnetic Field Twist Effect. *Soviet Astronomy* **1985**, *29*, 33–39.
42. Barnard, J.J. Probing the Magnetic Field of Radio Pulsars: A Reexamination of Polarization Position Angle Swings. *Astrophysical Journal* **1986**, *303*, 280. <https://doi.org/10.1086/164073>.
43. Blaskiewicz, M.; Cordes, J.M.; Wasserman, I. A Relativistic Model of Pulsar Polarization. *Astrophysical Journal* **1991**, *370*, 643. <https://doi.org/10.1086/169850>.
44. Hibschan, J.A.; Arons, J. Polarization Sweeps in Rotation-powered Pulsars. *Astrophysical Journal* **2001**, *546*, 382–393, [arXiv:astro-ph/astro-ph/0008117]. <https://doi.org/10.1086/318224>.
45. Gangadhara, R.T. Pulsar Radio Emission Altitude from Curvature Radiation. *Astrophysical Journal* **2004**, *609*, 335–339, [arXiv:astro-ph/astro-ph/0312081]. <https://doi.org/10.1086/420961>.
46. Yuen, R.; Melrose, D.B. Visibility of Pulsar Emission: Motion of the Visible Point. *Publications of the Astron. Soc. of Australia* **2014**, *31*, e039, [arXiv:astro-ph.SR/1409.1303]. <https://doi.org/10.1017/pasa.2014.35>.
47. Phillips, J.A. Radio Emission Altitudes in the Pulsar Magnetosphere. *Astrophysical Journal* **1992**, *385*, 282. <https://doi.org/10.1086/170936>.
48. Xilouris, K.M.; Kramer, M.; Jessner, A.; Wielebinski, R.; Timofeev, M. Emission properties of pulsars at mm-wavelengths. *Astronomy and Astrophysics* **1996**, *309*, 481–492.
49. Kijak, J.; Gil, J. Radio emission altitudes in pulsar magnetospheres. *Monthly Notices of the RAS* **1997**, *288*, 631–637. <https://doi.org/10.1093/mnras/288.3.631>.
50. von Hoensbroech, A.; Xilouris, K.M. Does radius-to-frequency mapping persist close to the pulsar surface? *Astronomy and Astrophysics* **1997**, *324*, 981–987.
51. Kijak, J.; Gil, J. Radio emission regions in pulsars. *Monthly Notices of the RAS* **1998**, *299*, 855–861. <https://doi.org/10.1046/j.1365-8711.1998.01832.x>.

52. Mitra, D.; Rankin, J.M. Toward an Empirical Theory of Pulsar Emission. VII. On the Spectral Behavior of Conal Beam Radii and Emission Heights. *Astrophysical Journal* **2002**, *577*, 322–336, [arXiv:astro-ph/0205356]. <https://doi.org/10.1086/342136>.
53. Kijak, J.; Gil, J. Radio emission altitude in pulsars. *Astronomy and Astrophysics* **2003**, *397*, 969–972. <https://doi.org/10.1051/0004-6361:20021583>.
54. Mitra, D.; Li, X.H. Comparing geometrical and delay radio emission heights in pulsars. *Astronomy and Astrophysics* **2004**, *421*, 215–228, [arXiv:astro-ph/astro-ph/0312560]. <https://doi.org/10.1051/0004-6361:20034094>.
55. Weltevrede, P.; Johnston, S. Profile and polarization characteristics of energetic pulsars. *Monthly Notices of the RAS* **2008**, *391*, 1210–1226, [arXiv:astro-ph/0809.2438]. <https://doi.org/10.1111/j.1365-2966.2008.13950.x>.
56. Mitra, D.; Rankin, J.M. Toward an Empirical Theory of Pulsar Emission. IX. On the Peculiar Properties and Geometric Regularity of Lyne and Manchester’s “PARTIAL Cone” Pulsars. *Astrophysical Journal* **2011**, *727*, 92, [arXiv:astro-ph.GA/1011.0556]. <https://doi.org/10.1088/0004-637X/727/2/92>.
57. Mitra, D.; Melikidze, G.I.; Basu, R. Meterwavelength Single Pulse Polarimetric Emission Survey. VI. Toward Understanding the Phenomenon of Pulsar Polarization in Partially Screened Vacuum Gap Model. *Astrophysical Journal* **2023**, *952*, 151, [arXiv:astro-ph.HE/2306.02537]. <https://doi.org/10.3847/1538-4357/acdc28>.
58. Posselt, B.; Karastergiou, A.; Johnston, S.; Parthasarathy, A.; Oswald, L.S.; Main, R.A.; Basu, A.; Keith, M.J.; Song, X.; Weltevrede, P.; et al. The Thousand Pulsar Array program on MeerKAT - IX. The time-averaged properties of the observed pulsar population. *Monthly Notices of the RAS* **2023**, *520*, 4582–4600, [arXiv:astro-ph.HE/2211.11849]. <https://doi.org/10.1093/mnras/stac3383>.
59. Cheng, A.F.; Ruderman, M.A. A theory of subpulse polarization patterns from radio pulsars. *Astrophysical Journal* **1979**, *229*, 348–360. <https://doi.org/10.1086/156959>.
60. Helfand, D.J.; Gotthelf, E.V.; Halpern, J.P. Vela Pulsar and Its Synchrotron Nebula. *Astrophysical Journal* **2001**, *556*, 380–391, [arXiv:astro-ph/astro-ph/0007310]. <https://doi.org/10.1086/321533>.
61. Lai, D.; Chernoff, D.F.; Cordes, J.M. Pulsar Jets: Implications for Neutron Star Kicks and Initial Spins. *Astrophysical Journal* **2001**, *549*, 1111–1118, [arXiv:astro-ph/astro-ph/0007272]. <https://doi.org/10.1086/319455>.
62. Johnston, S.; Hobbs, G.; Vigeland, S.; Kramer, M.; Weisberg, J.M.; Lyne, A.G. Evidence for alignment of the rotation and velocity vectors in pulsars. *Monthly Notices of the RAS* **2005**, *364*, 1397–1412, [arXiv:astro-ph/astro-ph/0510260]. <https://doi.org/10.1111/j.1365-2966.2005.09669.x>.
63. Rankin, J.M. Further Evidence for Alignment of the Rotation and Velocity Vectors in Pulsars. *Astrophysical Journal* **2007**, *664*, 443–447. <https://doi.org/10.1086/519018>.
64. Noutsos, A.; Kramer, M.; Carr, P.; Johnston, S. Pulsar spin-velocity alignment: further results and discussion. *Monthly Notices of the RAS* **2012**, *423*, 2736–2752, [arXiv:astro-ph.GA/1205.2305]. <https://doi.org/10.1111/j.1365-2966.2012.21083.x>.
65. Pulsar spin-velocity alignment: kinematic ages, birth periods and braking indices. *Monthly Notices of the RAS* **2013**, *430*, 2281–2301, [arXiv:astro-ph.GA/1301.1265]. <https://doi.org/10.1093/mnras/stt047>.
66. Force, M.M.; Demorest, P.; Rankin, J.M. Absolute polarization determinations of 33 pulsars using the Green Bank Telescope. *Monthly Notices of the RAS* **2015**, *453*, 4485–4499. <https://doi.org/10.1093/mnras/stv1709>.
67. Swarup, G.; Ananthakrishnan, S.; Kapahi, V.K.; Rao, A.P.; Subrahmanya, C.R.; Kulkarni, V.K. The Giant Metre-Wave Radio Telescope. *Current Science* **1991**, *60*, 95.
68. Gupta, Y.; Ajithkumar, B.; Kale, H.S.; Nayak, S.; Sabhapathy, S.; Sureshkumar, S.; Swami, R.V.; Chengalur, J.N.; Ghosh, S.K.; Ishwara-Chandra, C.H.; et al. The upgraded GMRT: opening new windows on the radio Universe. *Current Science* **2017**, *113*, 707–714. <https://doi.org/10.18520/cs/v113/i04/707-714>.
69. Johnston, S.; Kramer, M.; Karastergiou, A.; Keith, M.J.; Oswald, L.S.; Parthasarathy, A.; Weltevrede, P. The Thousand-Pulsar-Array programme on MeerKAT - XI. Application of the rotating vector model. *Monthly Notices of the RAS* **2023**, *520*, 4801–4814, [arXiv:astro-ph.HE/2212.03988]. <https://doi.org/10.1093/mnras/stac3636>.
70. Gil, J.A.; Lyne, A.G. Unravelling the position angle variations in PSR 0329+54. *Monthly Notices of the RAS* **1995**, *276*, L55–L57. <https://doi.org/10.1093/mnras/276.1.L55>.
71. Mitra, D.; Rankin, J.M.; Gupta, Y. Absolute broad-band polarization behaviour of PSR B0329+54: a glimpse of the core emission process. *Monthly Notices of the RAS* **2007**, *379*, 932–944, [arXiv:astro-ph/astro-ph/0701216]. <https://doi.org/10.1111/j.1365-2966.2007.11988.x>.
72. Lyne, A.G. Mode changing in pulsar radiation. *Monthly Notices of the RAS* **1971**, *153*, 27P. <https://doi.org/10.1093/mnras/153.1.27P>.
73. Bartel, N.; Morris, D.; Sieber, W.; Hankins, T.H. The mode-switching phenomenon in pulsars. *Astrophysical Journal* **1982**, *258*, 776–789. <https://doi.org/10.1086/160125>.
74. Chen, J.L.; Wang, H.G.; Wang, N.; Lyne, A.; Liu, Z.Y.; Jessner, A.; Yuan, J.P.; Kramer, M. Long-term Monitoring of Mode Switching for PSR B0329+54. *Astrophysical Journal* **2011**, *741*, 48, [arXiv:astro-ph.SR/1107.4676]. <https://doi.org/10.1088/0004-637X/741/1/48>.
75. Białkowski, S.; Lewandowski, W.; Kijak, J.; Błaszkiwicz, L.; Krankowski, A.; Osłowski, S. Mode switching characteristics of PSR B0329+54 at 150 MHz. *Astrophysics and Space Science* **2018**, *363*, 110. <https://doi.org/10.1007/s10509-018-3330-1>.
76. Brinkman, C.; Mitra, D.; Rankin, J. Investigation of the mode-switching phenomenon in pulsar B0329+54 through polarimetric analysis. *Monthly Notices of the RAS* **2019**, *484*, 2725–2734, [arXiv:astro-ph.HE/1901.08677]. <https://doi.org/10.1093/mnras/stz020>.

77. Mitra, D.; Gil, J.; Melikidze, G.I. Unraveling the Nature of Coherent Pulsar Radio Emission. *Astrophysical Journal, Letters* **2009**, *696*, L141–L145, [arXiv:astro-ph.HE/0903.3023]. <https://doi.org/10.1088/0004-637X/696/2/L141>.
78. Mitra, D.; Melikidze, G.I.; Basu, R. Evidence for Coherent Curvature Radiation in PSR J1645-0317 with Disordered Distribution of Polarization Position Angle. *Monthly Notices of the RAS* **2023**, [arXiv:astro-ph.HE/2302.08844]. <https://doi.org/10.1093/mnras/slad022>.
79. Smith, F.G. Relativistic Beaming of Radiation from Pulsars. *Nature* **1969**, *223*, 934–936. <https://doi.org/10.1038/223934a0>.
80. Smith, F.G. How Do Pulsars Pulse? *Quarterly Journal of the RAS* **1976**, *17*, 383.
81. Johnston, S.; Mitra, D.; Keith, M.J.; Oswald, L.S.; Karastergiou, A. The Thousand-Pulsar-Array programme on MeerKAT XIV: On the high linearly polarized pulsar signals. *Monthly Notices of the RAS* **2024**, [arXiv:astro-ph.HE/2404.10254]. <https://doi.org/10.1093/mnras/stae1175>.
82. Melikidze, G.I.; Mitra, D.; Gil, J. On the Adiabatic Walking of Plasma Waves in a Pulsar Magnetosphere. *Astrophysical Journal* **2014**, *794*, 105, [arXiv:astro-ph.SR/1409.1587]. <https://doi.org/10.1088/0004-637X/794/2/105>.
83. Morris, D.; Schwarz, U.J.; Cooke, D.J. Measurements of the Linear Polarization of Seven Pulsars at 11-cm Wavelength. *Astrophysics Letters* **1970**, *5*, 181.
84. Manchester, R.N.; Taylor, J.H.; Huguenin, G.R. Frequency Dependence of Pulsar Polarization. *Astrophysical Journal, Letters* **1973**, *179*, L7. <https://doi.org/10.1086/181105>.
85. McKinnon, M.M.; Stinebring, D.R. A Statistical Model for the Orthogonal Modes of Polarization in Pulsar Radio Emission. *Astrophysical Journal* **1998**, *502*, 883–897. <https://doi.org/10.1086/305924>.
86. Karastergiou, A.; Johnston, S.; Manchester, R.N. Polarization profiles of southern pulsars at 3.1 GHz. *Monthly Notices of the RAS* **2005**, *359*, 481–492, [arXiv:astro-ph/astro-ph/0502337]. <https://doi.org/10.1111/j.1365-2966.2005.08909.x>.
87. Wang, P.F.; Wang, C.; Han, J.L. On the frequency dependence of pulsar linear polarization. *Monthly Notices of the RAS* **2015**, *448*, 771–780, [arXiv:astro-ph.HE/1501.00066]. <https://doi.org/10.1093/mnras/stu2765>.
88. Gil, J.; Lyubarsky, Y.; Melikidze, G.I. Curvature Radiation in Pulsar Magnetospheric Plasma. *Astrophysical Journal* **2004**, *600*, 872–882, [arXiv:astro-ph/astro-ph/0310621]. <https://doi.org/10.1086/379972>.
89. Lominadze, D.G.; Machabeli, G.Z.; Melikidze, G.I.; Pataraiia, A.D. Plasma of pulsar magnetospheres. *Fizika Plazmy* **1986**, *12*, 1233–1249.
90. Rahaman, S.M.; Mitra, D.; Melikidze, G.I.; Lakoba, T. Pulsar radio emission mechanism - II. On the origin of relativistic Langmuir solitons in pulsar plasma. *Monthly Notices of the RAS* **2022**, *516*, 3715–3727. <https://doi.org/10.1093/mnras/stac2264>.
91. Gil, J.; Melikidze, G.I.; Geppert, U. Drifting subpulses and inner acceleration regions in radio pulsars. *Astronomy and Astrophysics* **2003**, *407*, 315–324, [arXiv:astro-ph/astro-ph/0305463]. <https://doi.org/10.1051/0004-6361:20030854>.
92. Rahaman, S.M.; Mitra, D.; Melikidze, G.I. Externally driven plasma models as candidates for pulsar radio emission. *Monthly Notices of the RAS* **2022**, *512*, 3589–3601, [arXiv:astro-ph.HE/2203.05396]. <https://doi.org/10.1093/mnras/stac696>.
93. Cordes, J.M.; Weisberg, J.M.; Hankins, T.H. Quasiperiodic Microstructure in Radio Pulsar Emission. *Astronomical Journal* **1990**, *100*, 1882. <https://doi.org/10.1086/115644>.
94. Mitra, D.; Arjunwadkar, M.; Rankin, J.M. Polarized Quasiperiodic Structures in Pulsar Radio Emission Reflect Temporal Modulations of Non-stationary Plasma Flow. *Astrophysical Journal* **2015**, *806*, 236, [arXiv:astro-ph.HE/1502.06897]. <https://doi.org/10.1088/0004-637X/806/2/236>.
95. Mikhailovskii, A.B.; Onishchenko, O.G.; Suramlishvili, G.I.; Sharapov, S.E. The Emergence of Electromagnetic Waves from Pulsar Magnetospheres. *Soviet Astronomy Letters* **1982**, *8*, 369–371.
96. Bjornsson, C.I. A new look at pulsar polarization. *Astrophysical Journal* **1984**, *277*, 367–374. <https://doi.org/10.1086/161703>.
97. Gil, J.A.; Snakowski, J.K. Curvature radiation and the core emission of pulsars. *Astronomy and Astrophysics* **1990**, *234*, 237–242.
98. Gil, J.A.; Snakowski, J.K. Pulsar emission as curvature-generated polarized shot noise. *Astronomy and Astrophysics* **1990**, *234*, 269.
99. Radhakrishnan, V.; Rankin, J.M. Toward an Empirical Theory of Pulsar Emission. V. On the Circular Polarization in Pulsar Radiation. *Astrophysical Journal* **1990**, *352*, 258. <https://doi.org/10.1086/168531>.
100. Michel, F.C. A Pulsar Emission Model: Observational Tests. *Astrophysical Journal* **1987**, *322*, 822. <https://doi.org/10.1086/165775>.
101. Gangadhara, R.T. Orthogonal polarization mode phenomenon in pulsars. *Astronomy and Astrophysics* **1997**, *327*, 155–166, [arXiv:astro-ph/astro-ph/9707168]. <https://doi.org/10.48550/arXiv.astro-ph/9707168>.
102. Petrova, S.A.; Lyubarskii, Y.E. Propagation effects in pulsar magnetospheres. *Astronomy and Astrophysics* **2000**, *355*, 1168–1180.
103. Wang, C.; Lai, D.; Han, J. Polarization changes of pulsars due to wave propagation through magnetospheres. *Monthly Notices of the RAS* **2010**, *403*, 569–588, [arXiv:astro-ph.HE/0910.2793]. <https://doi.org/10.1111/j.1365-2966.2009.16074.x>.
104. Allen, M.C.; Melrose, D.B. Elliptically polarized natural modes in pulsar magnetospheres. *Publications of the Astron. Soc. of Australia* **1982**, *4*, 365–370. <https://doi.org/10.1017/S1323358000021147>.
105. Shafranov, V.D. Electromagnetic Waves in a Plasma. *Reviews of Plasma Physics* **1967**, *3*, 1.
106. Radhakrishnan, V.; Cooke, D.J.; Komesaroff, M.M.; Morris, D. Evidence in Support of a Rotational Model for the Pulsar PSR 0833-45. *Nature* **1969**, *221*, 443–446. <https://doi.org/10.1038/221443a0>.
107. Backer, D.C. Pulsar average wave forms and hollow-cone beam models. *Astrophysical Journal* **1976**, *209*, 895–907. <https://doi.org/10.1086/154788>.
108. Gil, J.A.; Kijak, J.; Seiradakis, J.H. On the two-dimensional structure of pulsar beams. *Astronomy and Astrophysics* **1993**, *272*, 268–276.

109. Maciesiak, K.; Gil, J.; Ribeiro, V.A.R.M. On the pulse-width statistics in radio pulsars - I. Importance of the interpulse emission. *Monthly Notices of the RAS* **2011**, *414*, 1314–1328, [arXiv:astro-ph.GA/1102.3348]. <https://doi.org/10.1111/j.1365-2966.2011.18471.x>.
110. Maciesiak, K.; Gil, J. On the pulse-width statistics in radio pulsars - II. Importance of the core profile components. *Monthly Notices of the RAS* **2011**, *417*, 1444–1453, [arXiv:astro-ph.GA/1107.0212]. <https://doi.org/10.1111/j.1365-2966.2011.19359.x>.
111. Maciesiak, K.; Gil, J.; Melikidze, G. On the pulse-width statistics in radio pulsars - III. Importance of the conal profile components. *Monthly Notices of the RAS* **2012**, *424*, 1762–1773, [arXiv:astro-ph.GA/1205.1297]. <https://doi.org/10.1111/j.1365-2966.2012.21246.x>.
112. Skrzypczak, A.; Basu, R.; Mitra, D.; Melikidze, G.I.; Maciesiak, K.; Koralewska, O.; Filothodoros, A. Meterwavelength Single-pulse Polarimetric Emission Survey. IV. The Period Dependence of Component Widths of Pulsars. *Astrophysical Journal* **2018**, *854*, 162, [arXiv:astro-ph.HE/1801.02720]. <https://doi.org/10.3847/1538-4357/aaa758>.
113. Lyne, A.G.; Manchester, R.N. The shape of pulsar radio beams. *Monthly Notices of the RAS* **1988**, *234*, 477–508. <https://doi.org/10.1093/mnras/234.3.477>.
114. Basu, R.; Mitra, D.; Rankin, J.M. Toward an Empirical Theory of Pulsar Emission. X. On the Precursor and Postcursor Emission. *Astrophysical Journal* **2015**, *798*, 105, [arXiv:astro-ph.GA/1411.0117]. <https://doi.org/10.1088/0004-637X/798/2/105>.
115. Dyks, J.; Rudak, B. Asymmetry of bifurcated features in radio pulsar profiles. *Monthly Notices of the RAS* **2012**, *420*, 3403–3411, [arXiv:astro-ph.HE/1204.0452]. <https://doi.org/10.1111/j.1365-2966.2011.20265.x>.
116. Wang, H.G.; Pi, F.P.; Zheng, X.P.; Deng, C.L.; Wen, S.Q.; Ye, F.; Guan, K.Y.; Liu, Y.; Xu, L.Q. A Fan Beam Model for Radio Pulsars. I. Observational Evidence. *Astrophysical Journal* **2014**, *789*, 73, [arXiv:astro-ph.HE/1405.6825]. <https://doi.org/10.1088/0004-637X/789/1/73>.
117. Dyks, J.; Rudak, B. The origin of the frequency-dependent behaviour of pulsar radio profiles. *Monthly Notices of the RAS* **2015**, *446*, 2505–2522, [arXiv:astro-ph.SR/1411.0866]. <https://doi.org/10.1093/mnras/stu2262>.
118. Karastergiou, A.; Johnston, S. An empirical model for the beams of radio pulsars. *Monthly Notices of the RAS* **2007**, *380*, 1678–1684, [arXiv:astro-ph/0707.2547]. <https://doi.org/10.1111/j.1365-2966.2007.12237.x>.
119. Basu, R.; Mitra, D.; Melikidze, G.I.; Skrzypczak, A. Classification of subpulse drifting in pulsars. *Monthly Notices of the RAS* **2019**, *482*, 3757–3788, [arXiv:astro-ph.HE/1810.08423]. <https://doi.org/10.1093/mnras/sty2846>.
120. Rankin, J. Radio pulsar beam geometry at lower frequencies: bright sources outside the Arecibo sky. *Monthly Notices of the RAS* **2022**, *514*, 3202–3211, [arXiv:astro-ph.HE/2206.07739]. <https://doi.org/10.1093/mnras/stac1302>.
121. Gil, J.A.; Sendyk, M. Spark Model for Pulsar Radiation Modulation Patterns. *Astrophysical Journal* **2000**, *541*, 351–366, [arXiv:astro-ph/astro-ph/0002450]. <https://doi.org/10.1086/309394>.
122. Maron, O.; Kijak, J.; Kramer, M.; Wielebinski, R. Pulsar spectra of radio emission. *Astronomy and Astrophysics, Supplement* **2000**, *147*, 195–203, [arXiv:astro-ph/astro-ph/0010233]. <https://doi.org/10.1051/aas:2000298>.
123. Jankowski, F.; van Straten, W.; Keane, E.F.; Bailes, M.; Barr, E.D.; Johnston, S.; Kerr, M. Spectral properties of 441 radio pulsars. *Monthly Notices of the RAS* **2018**, *473*, 4436–4458, [arXiv:astro-ph.HE/1709.08864]. <https://doi.org/10.1093/mnras/stx2476>.
124. Rickett, B.J. Radio propagation through the turbulent interstellar plasma. *Annual Review of Astron and Astrophysics* **1990**, *28*, 561–605. <https://doi.org/10.1146/annurev.aa.28.090190.003021>.
125. Helfand, D.J.; Fowler, L.A.; Kuhlman, J.V. Pulsar flux observations: long-term intensity and spectral variations. *Astronomical Journal* **1977**, *82*, 701–705. <https://doi.org/10.1086/112110>.
126. Kaspi, V.M.; Stinebring, D.R. Long-Term Pulsar Flux Monitoring and Refractive Interstellar Scintillation. *Astrophysical Journal* **1992**, *392*, 530. <https://doi.org/10.1086/171454>.
127. Labrecque, D.R.; Rankin, J.M.; Cordes, J.M. Long-Term Intensity Variations of 20 Pulsars. *Astronomical Journal* **1994**, *108*, 1854. <https://doi.org/10.1086/117198>.
128. Stinebring, D.R.; Smirnova, T.V.; Hankins, T.H.; Hovis, J.S.; Kaspi, V.M.; Kempner, J.C.; Myers, E.; Nice, D.J. Five Years of Pulsar Flux Density Monitoring: Refractive Scintillation and the Interstellar Medium. *Astrophysical Journal* **2000**, *539*, 300–316. <https://doi.org/10.1086/309201>.
129. Kumamoto, H.; Dai, S.; Johnston, S.; Kerr, M.; Shannon, R.M.; Weltevrede, P.; Sobey, C.; Manchester, R.N.; Hobbs, G.; Takahashi, K. Flux density variability of 286 radio pulsars from a decade of monitoring. *Monthly Notices of the RAS* **2021**, *501*, 4490–4513, [arXiv:astro-ph.HE/2012.08119]. <https://doi.org/10.1093/mnras/staa3910>.
130. Lewandowski, W.; Kowalińska, M.; Kijak, J. The analysis of the largest sample of multifrequency pulsar scatter time estimates. *Monthly Notices of the RAS* **2015**, *449*, 1570–1583, [arXiv:astro-ph.SR/1502.06330]. <https://doi.org/10.1093/mnras/stv385>.
131. Basu, R.; Mitra, D.; Melikidze, G.I. Spectral Variation across Pulsar Profile due to Coherent Curvature Radiation. *Astrophysical Journal* **2022**, *927*, 208, [arXiv:astro-ph.HE/2201.11398]. <https://doi.org/10.3847/1538-4357/ac5039>.
132. Cheng, A.F.; Ruderman, M.A. Particle acceleration and radio emission above pulsar polar caps. *Astrophysical Journal* **1980**, *235*, 576–586. <https://doi.org/10.1086/157661>.
133. Jones, P.B. Properties of condensed matter in very strong magnetic fields. *Monthly Notices of the RAS* **1986**, *218*, 477–485. <https://doi.org/10.1093/mnras/218.3.477>.
134. Basu, R.; Mitra, D.; Melikidze, G.I. Estimating the Evolution of Sparks in the Partially Screened Gap of Pulsars from Subpulse Drifting. *Astrophysical Journal* **2023**, *947*, 86, [arXiv:astro-ph.HE/2303.12229]. <https://doi.org/10.3847/1538-4357/acc6c6>.

135. Backer, D.C. Pulsar Fluctuation Spectra and the Generalized Drifting-Subpulse Phenomenon. *Astrophysical Journal* **1973**, *182*, 245–276. <https://doi.org/10.1086/152134>.
136. Weltevrede, P.; Edwards, R.T.; Stappers, B.W. The subpulse modulation properties of pulsars at 21 cm. *Astronomy and Astrophysics* **2006**, *445*, 243–272, [arXiv:astro-ph/astro-ph/0507282]. <https://doi.org/10.1051/0004-6361:20053088>.
137. Basu, R.; Mitra, D.; Melikidze, G.I.; Maciesiak, K.; Skrzypczak, A.; Szary, A. Meterwavelength Single-pulse Polarimetric Emission Survey. II. the Phenomenon of Drifting Subpulses. *Astrophysical Journal* **2016**, *833*, 29, [arXiv:astro-ph.HE/1608.00050]. <https://doi.org/10.3847/1538-4357/833/1/29>.
138. Drake, F.D.; Craft, H.D. Second Periodic Pulsation in Pulsars. *Nature* **1968**, *220*, 231–235. <https://doi.org/10.1038/220231a0>.
139. Backer, D.C.; Rankin, J.M.; Campbell, D.B. Pulsar fluctuation spectra and the generalized drifting-subpulse phenomenon. II. *Astrophysical Journal* **1975**, *197*, 481–487. <https://doi.org/10.1086/153533>.
140. Basu, R.; Mitra, D.; Melikidze, G.I. Periodic Modulation: Newly Emergent Emission Behavior in Pulsars. *Astrophysical Journal* **2020**, *889*, 133, [arXiv:astro-ph.HE/1912.06868]. <https://doi.org/10.3847/1538-4357/ab63c9>.
141. Basu, R.; Paul, A.; Mitra, D. Subpulse drifting, nulling, and mode changing in PSR J2006 - 0807 with core emission. *Monthly Notices of the RAS* **2019**, *486*, 5216–5230, [arXiv:astro-ph.HE/1904.13202]. <https://doi.org/10.1093/mnras/stz1225>.
142. Basu, R.; Lewandowski, W.; Kijak, J. Subpulse drifting and periodic nulling in single pulse emission of PSR B2000+40. *Monthly Notices of the RAS* **2020**, *499*, 906–913, [arXiv:astro-ph.HE/2008.03329]. <https://doi.org/10.1093/mnras/staa2398>.
143. Rahaman, S.k.M.; Basu, R.; Mitra, D.; Melikidze, G.I. Mode changing, subpulse drifting, and nulling in four component conal pulsar PSR J2321+6024. *Monthly Notices of the RAS* **2021**, *500*, 4139–4152, [arXiv:astro-ph.HE/2011.05214]. <https://doi.org/10.1093/mnras/staa3518>.
144. Wen, Z.G.; Yuan, J.P.; Wang, N.; Li, D.; Chen, J.L.; Wang, P.; Wu, Q.D.; Yan, W.M.; Yuen, R.; Wang, Z.; et al. A Single-pulse Study of the Subpulse Drifter PSR J1631+1252 Discovered at FAST. *Astrophysical Journal* **2022**, *929*, 71. <https://doi.org/10.3847/1538-4357/ac5d5d>.
145. Szary, A.; van Leeuwen, J.; Wright, G.; Weltevrede, P.; Agar, C.H.; Tiburzi, C.; Maan, Y.; Keith, M.J. MeerKAT Observations of the Reversing Drifting Subpulses in PSR J1750-3503. *Astrophysical Journal* **2022**, *934*, 23, [arXiv:astro-ph.HE/2206.02382]. <https://doi.org/10.3847/1538-4357/ac75e2>.
146. Wang, H.; Wen, Z.G.; Duan, X.F.; Wang, Z.; He, D.L.; Wang, H.G.; Wang, N.; Yuan, J.P.; Yan, W.M.; Yuen, R.; et al. Exploring the Individual Pulse Behavior of Pulsar J1701-3726 with Parkes. *Astrophysical Journal* **2023**, *950*, 166. <https://doi.org/10.3847/1538-4357/acd17b>.
147. Basu, R.; Lewandowski, W.; Kijak, J.; Bartosz, Ś.; Soida, M.; Błaszkiwicz, L.; Krankowski, A. Single pulse emission from PSR B0809+74 at 150 MHz using Polish LOFAR station. *Monthly Notices of the RAS* **2023**, *526*, 691–699, [arXiv:astro-ph.HE/2309.03820]. <https://doi.org/10.1093/mnras/stad2737>.
148. Yan, Y.; Han, J.L.; Wang, C.; Wang, P.F. Quasi-regular variations of subpulse drifting for PSR J1857+0057. *Monthly Notices of the RAS* **2023**, *526*, 3184–3200, [arXiv:astro-ph.HE/2310.00649]. <https://doi.org/10.1093/mnras/stad2983>.
149. Song, X.; Weltevrede, P.; Szary, A.; Wright, G.; Keith, M.J.; Basu, A.; Johnston, S.; Karastergiou, A.; Main, R.A.; Oswald, L.S.; et al. The Thousand-Pulsar-Array programme on MeerKAT - VIII. The subpulse modulation of 1198 pulsars. *Monthly Notices of the RAS* **2023**, *520*, 4562–4581, [arXiv:astro-ph.HE/2301.04067]. <https://doi.org/10.1093/mnras/stad135>.
150. Lakoba, T.; Mitra, D.; Melikidze, G. Relativistic charge solitons created due to non-linear Landau damping: a candidate for explaining coherent radio emission in pulsars. *Monthly Notices of the RAS* **2018**, *480*, 4526–4543, [arXiv:astro-ph.HE/1808.03657]. <https://doi.org/10.1093/mnras/sty2152>.
151. Johnston, S.; Kramer, M. On the beam properties of radio pulsars with interpulse emission. *Monthly Notices of the RAS* **2019**, *490*, 4565–4574, [arXiv:astro-ph.HE/1910.04550]. <https://doi.org/10.1093/mnras/stz2865>.
152. Basu, R.; Mitra, D.; Melikidze, G.I. Search for Off-pulse Emission in Long-period Pulsars. *Astrophysical Journal* **2020**, *905*, 30, [arXiv:astro-ph.HE/2010.09397]. <https://doi.org/10.3847/1538-4357/abc3c7>.
153. Yuan, M.; Zhu, W.; Kramer, M.; Peng, B.; Lu, J.; Xu, R.; Shao, L.; Wang, H.G.; Meng, L.; Niu, J.; et al. High-altitude Magnetospheric Emissions from Two Pulsars. *Astrophysical Journal* **2023**, *949*, 115, [arXiv:astro-ph.HE/2306.04935]. <https://doi.org/10.3847/1538-4357/accb9a>.
154. Hermsen, W.; Kuiper, L.; Basu, R.; Hessels, J.W.T.; Mitra, D.; Rankin, J.M.; Stappers, B.W.; Wright, G.A.E.; Griefsmeier, J.M.; Serylak, M.; et al. Discovery of synchronous X-ray and radio moding of PSR B0823+26. *Monthly Notices of the RAS* **2018**, *480*, 3655–3670, [arXiv:astro-ph.HE/1808.01901]. <https://doi.org/10.1093/mnras/sty2075>.
155. Chen, X.; Yan, Y.; Han, J.L.; Wang, C.; Wang, P.F.; Jing, W.C.; Lee, K.J.; Zhang, B.; Xu, R.X.; Wang, T.; et al. Strong and weak pulsar radio emission due to thunderstorms and raindrops of particles in the magnetosphere. *Nature Astronomy* **2023**, *7*, 1235–1244, [arXiv:astro-ph.HE/2306.12017]. <https://doi.org/10.1038/s41550-023-02056-z>.
156. Yan, Y.; Han, J.L.; Zhou, D.J.; Xie, L.; Kou, F.F.; Wang, P.F.; Wang, C.; Wang, T. Dwarf pulses of ten pulsars detected by FAST. *arXiv e-prints* **2024**, p. arXiv:2403.01084, [arXiv:astro-ph.HE/2403.01084].
157. Kramer, M.; Xilouris, K.M.; Lorimer, D.R.; Doroshenko, O.; Jessner, A.; Wielebinski, R.; Wolszczan, A.; Camilo, F. The Characteristics of Millisecond Pulsar Emission. I. Spectra, Pulse Shapes, and the Beaming Fraction. *Astrophysical Journal* **1998**, *501*, 270–285, [arXiv:astro-ph/astro-ph/9801177]. <https://doi.org/10.1086/305790>.

158. Kramer, M.; Lange, C.; Lorimer, D.R.; Backer, D.C.; Xilouris, K.M.; Jessner, A.; Wielebinski, R. The Characteristics of Millisecond Pulsar Emission. III. From Low to High Frequencies. *Astrophysical Journal* **1999**, *526*, 957–975, [arXiv:astro-ph/astro-ph/9906442]. <https://doi.org/10.1086/308042>.
159. Xilouris, K.M.; Kramer, M.; Jessner, A.; von Hoensbroech, A.; Lorimer, D.R.; Wielebinski, R.; Wolszczan, A.; Camilo, F. The Characteristics of Millisecond Pulsar Emission. II. Polarimetry. *Astrophysical Journal* **1998**, *501*, 286–306, [arXiv:astro-ph/astro-ph/9801178]. <https://doi.org/10.1086/305791>.
160. Turolla, R.; Zane, S.; Watts, A.L. Magnetars: the physics behind observations. A review. *Reports on Progress in Physics* **2015**, *78*, 116901, [arXiv:astro-ph.HE/1507.02924]. <https://doi.org/10.1088/0034-4885/78/11/116901>.

**Disclaimer/Publisher’s Note:** The statements, opinions and data contained in all publications are solely those of the individual author(s) and contributor(s) and not of MDPI and/or the editor(s). MDPI and/or the editor(s) disclaim responsibility for any injury to people or property resulting from any ideas, methods, instructions or products referred to in the content.